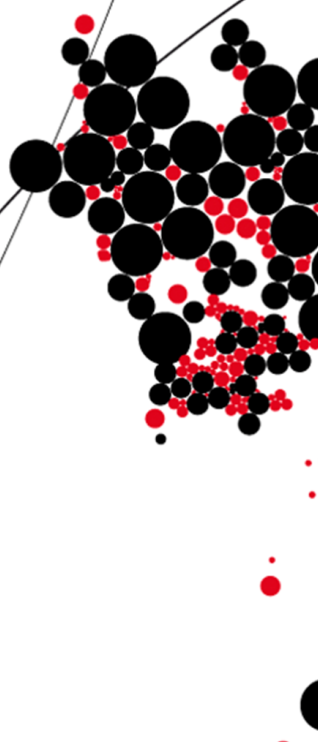




UNIVERSITY OF TWENTE.

Faculty of Engineering Technology



Improvement of longitudinal tracking and the addition of turning control of an underactuated moment exchange unicycle robot

Frederik B. Koopman

M.Sc. Thesis

May 21, 2019

ET.19/TM-5854

Supervisors:

Prof.dr.ir. A. de Boer

Dr. ir. R.G.K.M. Aarts

Other exam committee members:

prof.dr.ing. B. Rosic

dr. I.S.M. Khalil

Faculty of Engineering Technology
Structural Dynamics, Acoustics & Control
University of Twente
P.O. Box 217
7500 AE Enschede
The Netherlands

Preface

From a young age I always said I wanted to become an inventor, so the choice of studying mechanical engineering was obvious step. During my studentship I developed even greater passion for mechatronic systems, thus when I was presented with this graduation assignment I jumped straight in.

I hope that reading this report will give you, the reader, new insights and knowledge as the research I have done for it has given me.

I would like to thank my supervisor R.G.K.M. Aarts for his guidance during this thesis, both in giving me new insights and looking at some problems from a different and/or more complete angle. As well as putting up with my broken English texts due to my dyslexia. Also I want to thank L. Tiemersma and E. Molenkamp for helping me with making and/or repairing the moment exchange unicycle robot.

Summary

Nowadays more and more packages are being send. This could be automated by delivery drones. The moment exchange unicycle robot could be one of these drones. For this drone to work it needs to have good controllability, thus good tracking, and capable of turning. To get better tracking a feedforward controller was added parallel to the cascaded feedback controller for the driving direction. This controller is of the acceleration feedforward type, thus it is a function of the reference profile acceleration and it results in a pitch angle. The controller was validated by simulations and experiments and found to perform well. Its performance is limited by underactuation and the assumption of a constant acceleration. The addition of turning control was done by implementing a control strategy found in literature. This strategy applies a harmonic reference to both the roll and pitch angles. The sinuses are in-phase or in counter-phase depending on which direction the drone should turn. The higher the amplitude of the sinuses the faster the drone will turn. From simulations and experiments it was found that this strategy works. Also, the simulation model was compared to the experimental setup found to behave similar.

Contents

Preface	iii
Summary	v
Lists of acronyms	ix
1 Introduction	1
1.1 Motivation	1
1.2 Framework	2
1.3 Goals of the assignment and research questions	2
1.4 Report organization	3
2 Moment Exchange Unicycle Robot (MEUR)	5
2.1 Coordinate system and bodies	5
2.2 Control	6
2.3 Sensor setup	9
3 Simulation model	11
3.1 SPACAR model	11
3.2 Model comparison to experimental setup	11
4 Experimental setup	13
4.1 Existing setup	13
4.2 New Setup	13
5 Improved longitudinal tracking	15
5.1 Derivation	16
5.2 Validation with simulations	16
5.3 Experimental validation	18
6 Cornering and turning	19
6.1 Cornering	19
6.2 Turning	21
6.2.1 Simulated jaw plant identification	22
6.2.2 Simulated jaw Proportional and Derivative controller (PD) stability check	24

6.2.3	Simulation	25
6.2.4	Experiments	27
6.2.5	Experimental jaw plant identification	28
6.2.6	Jaw PD stability check experimental setup	29
6.3	Reflection	30
7	Conclusions and recommendations	31
7.1	Conclusions	31
7.1.1	Model comparison to experimental setup	31
7.1.2	Experimental setup	31
7.1.3	Improved longitudinal tracking	31
7.1.4	Cornering and turning	31
7.2	Recommendations	32
7.2.1	Replace the roll and pitch Sliding Mode Controller (SMC) by a different controller	32
7.2.2	Investigate the influence of the sinus frequency of the jaw Single input Multiple output (system) (SiMo)	33
7.2.3	Investigate the influence of different gains of the SiMo on the roll and pitch	33
7.2.4	Optimize the jaw PD	33
7.2.5	Design and construct a new MEUR	34
7.2.6	Investigate a coupled movement with longitudinal movement and turning	34
7.2.7	Design an extra outer loop controller to navigate and control the MEUR through the real world	34
	References	35
	Appendices	
A	SPACAR model MEUR	37
B	New experimental setup	39
B.1	Wishes and requirements	39
B.2	Design choices and process	41
C	Derivation ideal roll angle during cornering	45
D	Evaluation of the reaction wheel	47
D.1	Derivation	47
D.2	Validation	51
D.3	Reaction wheel alteration	52

Lists of acronyms

Controllers

P	Proportional controller
PD	Proportional and Derivative controller
PI	Proportional and Integral controller
PID	Proportional, Integral and Derivative controller
SMC	Sliding Mode Controller

Dynamics

DOF	Degree Of Freedom
EMF	ElectroMotive Force
SiMo	Single input Multiple output (system)

Electronics

ADC	Analog to Digital Converter
CPLD	Complex Programmable Logic Device
DAC	Digital to Analog Converter
FPGA	Field Programmable Gate Array
PCB	Printed Circuit Board
VHDL	Very high speed integrated circuit Hardware Description Language

Other

MEUR Moment Exchange Unicycle Robot

SDAC Structural Dynamics, Acoustics & Control

Introduction

Nowadays more and more packages are being send. The task of delivery of these packages is very well suited to be automated. Multiple organizations, governments and companies are already experimenting with delivery drones. Nearly all these experiments are done with flying drones. Although these drones are not bound to roads and much faster than wheeled drones, they offer more safety risks and there could be places where they are not allowed to operate due to airspace restrictions.

One robot possible capable for a role as a delivery drone task is the Moment Exchange Unicycle Robot (MEUR). The MEUR, see figure 1.1, is a single wheel robot with a reaction wheel placed perpendicular to the drive wheel. This setup allows the robot to keep itself upright. Compared to other wheeled drones the MEUR has the advantage that it has a very small footprint. Therefore, it takes up less space on the already busy roads. Another advantage is the ability to remain upright while driving over sloped and uneven surfaces [3]. An impression of the the MEUR as a delivery drone is the transwheel delivery drone concept which is displayed in figure 1.2.

1.1 Motivation

Prior to this thesis a MEUR has been developed at the University of Twente that was capable of moving back and forth over flat and sloped surfaces [3]. However, it is found that two improvements need to be

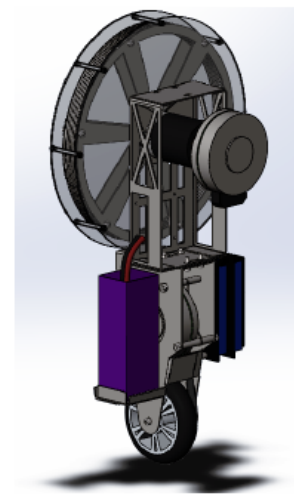


Figure 1.1: MEUR [1]–[3]



Figure 1.2: Transwheel delivery drone concept [4]

made for this robot to be more suited to fulfill the role of delivery drone. First of all, better longitudinal tracking of the MEUR, thus following a reference with a smaller error, will result in a better controllable drone. Secondly, it should be capable of either making corners or turning. The difference between cornering and turning is that with cornering the MEUR follows a (circular) path. While with turning the MEUR remains in its place. In figures 1.3 and 1.4 this is shown to make this concept more clear, where in both cases the MEUR starts in position and orientation 1 and ends in 2.

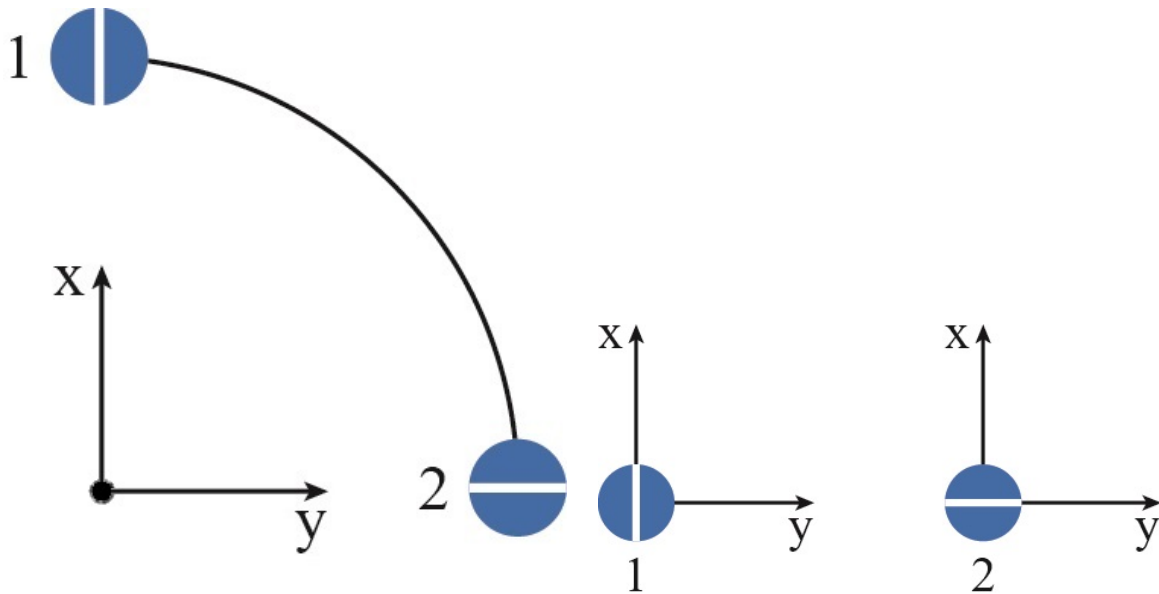


Figure 1.3: Cornering path top view

Figure 1.4: Turning begin and end situation top view

1.2 Framework

The research for this thesis was done at the University of Twente in the Structural Dynamics, Acoustics & Control (SDAC) research group. The MEUR has been developed and used by previous students [1]–[3], [5].

1.3 Goals of the assignment and research questions

This master thesis has the following goals:

1. Improving longitudinal tracking of the MEUR
2. Adding corner or turning control to the MEUR

These goals lead to the following research questions and subquestions.

1. Is it possible to improve the longitudinal tracking of the MEUR? And how?
 - Is feedforward in the longitudinal direction possible on the MEUR? And how?
2. Is it possible to add either cornering or turning control to the MEUR? And how?
 - Can the MEUR perform corners? And how?
 - Can the MEUR perform turning? And how?

1.4 Report organization

This document has the following structure. First the MEUR is introduced in more detail in Chapter 2. In Chapter 3 it is explained how a model was made for the simulations. Chapter 4 will address the experimental setup. Then, in Chapter 5 the improved longitudinal tracking will be addressed. Chapter 6 will go into detail on the cornering and turning control. Finally, in Chapter 7 the conclusions and recommendations are given.

During this thesis I have among other things contributed the following to the MEUR project:

1. Edited Langius [6] presented SPACAR model to match the real life MEUR
2. Made the MEUR wireless
3. Derived a feedforward controller to improve longitudinal tracking
4. Implemented Majima control strategy for turning
5. Tested Majima control strategy in experiments
6. Turning plant identification
7. Several simulations and experiments comparisons
8. Derivation of ideal roll angle during cornering
9. Evaluation of the reaction wheel

MEUR

2.1 Coordinate system and bodies

The coordinate system used in this thesis report is the same as used before by the previous students working on the MEUR [3], [6]. This coordinate system and axis definitions is illustrated in figures 2.1 and 2.2.

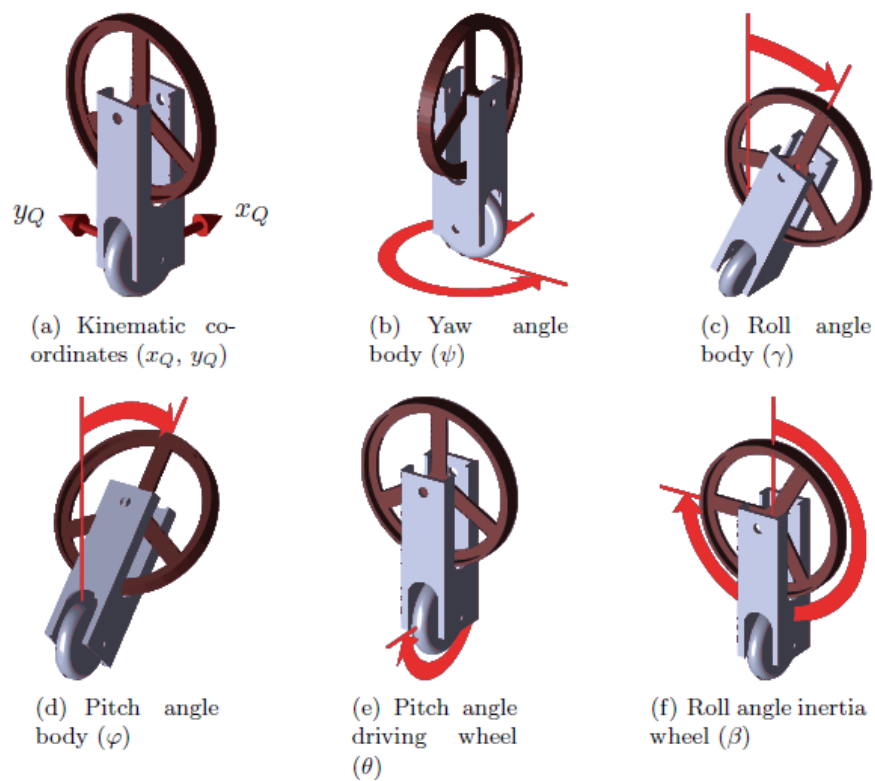


Figure 2.1: Coordinate system [6]

As already stated a MEUR is a single wheel robot with a reaction wheel placed perpendicular to the drive wheel. From the rendering, see figure 2.3, the MEUR can be seen as three bodies. Namely the frame or main body, the driving wheel and the reaction wheel. The MEUR has two motors to drive the driving and reaction wheels. The bodies are connected to each other and the fixed world with the following; the driving wheel has a contact point with the fixed world; the driving wheel is connected to the frame with a hinge; the reaction wheel is connected to the frame with a hinge.

The contact point between the driving wheel and the fixed world fixes the vertical movement of the MEUR. Also it has a no slip condition with the ground thus linking its rotation θ and the longitudinal direction X and fixes Y . Additionally the contact point adds friction in the jaw direction. The hinge between the driving wheel and the frame only allows for one Degree Of Freedom (DOF) namely a rotation in the XZ plane, i.e. pitch. The motor driving the driving wheel acts also on this hinge. The second hinge connecting the reaction wheel and the frame also has one DOF. The rotation is in the YZ plane, i.e. roll. The reaction wheel motor acts on this hinge.

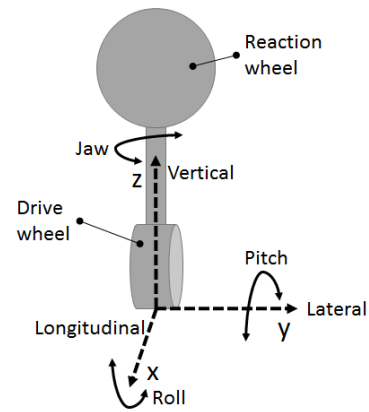


Figure 2.2: Axis definitions [3]

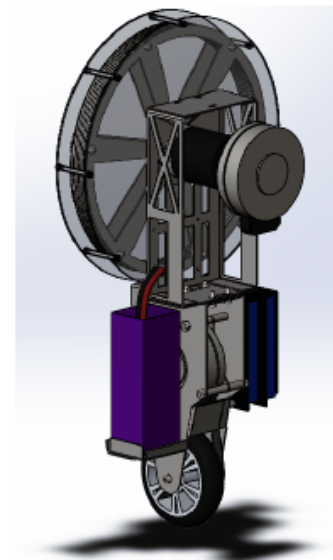


Figure 2.3: MEUR [1]–[3]

2.2 Control

The controller for the MEUR has been designed by De Vries [3] by first assuming the dynamics of the MEUR can be seen as two uncoupled 2D systems. Namely the lateral and longitudinal 2D systems [3, Appendix E], see figures 2.4 and 2.5 for their schematic representation.

Then controllers are designed for both systems and these are combined into the controller for the MEUR. The controller is schematically represented in figure 2.6. The signals in this figure can be only position signals but also their derivatives. These are left out to retain a readable figure. The parameter r_{DW} is the radius of the driving wheel. From the figure it is clear that the controller assumes an uncoupled system since there are no connections between the lateral and longitudinal controllers.

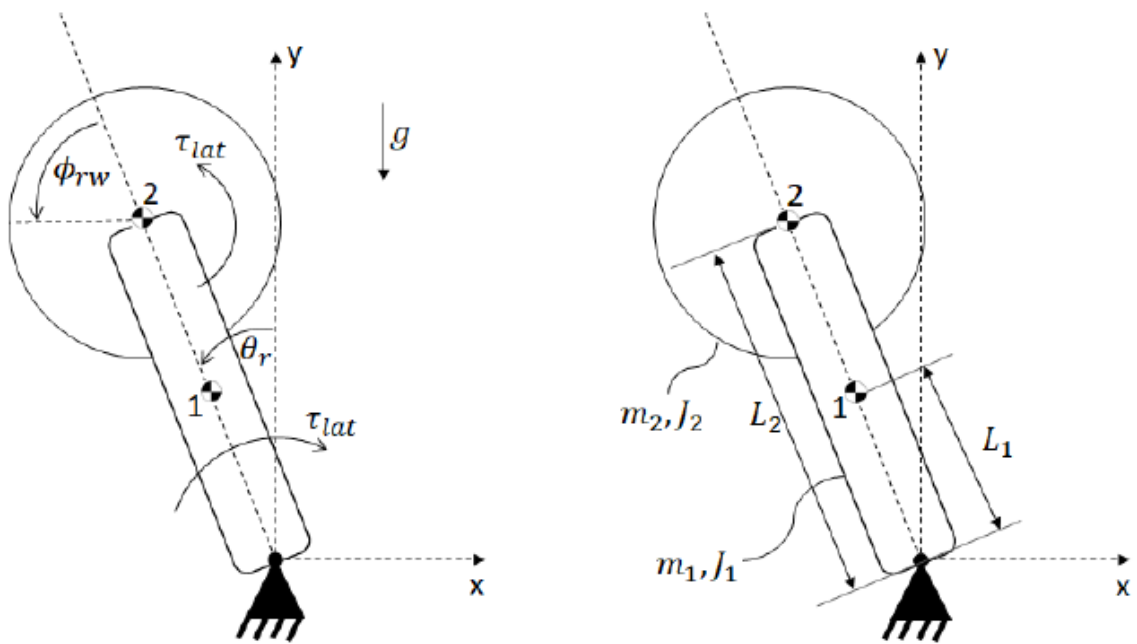


Figure 2.4: Schematic representation of the lateral system [3]

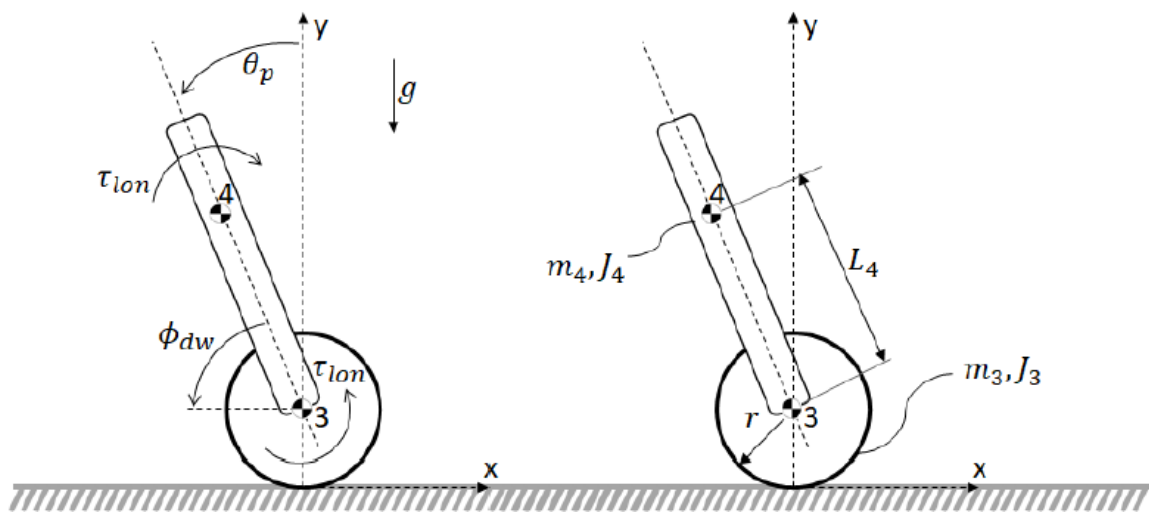


Figure 2.5: Schematic representation of the longitudinal system [3]

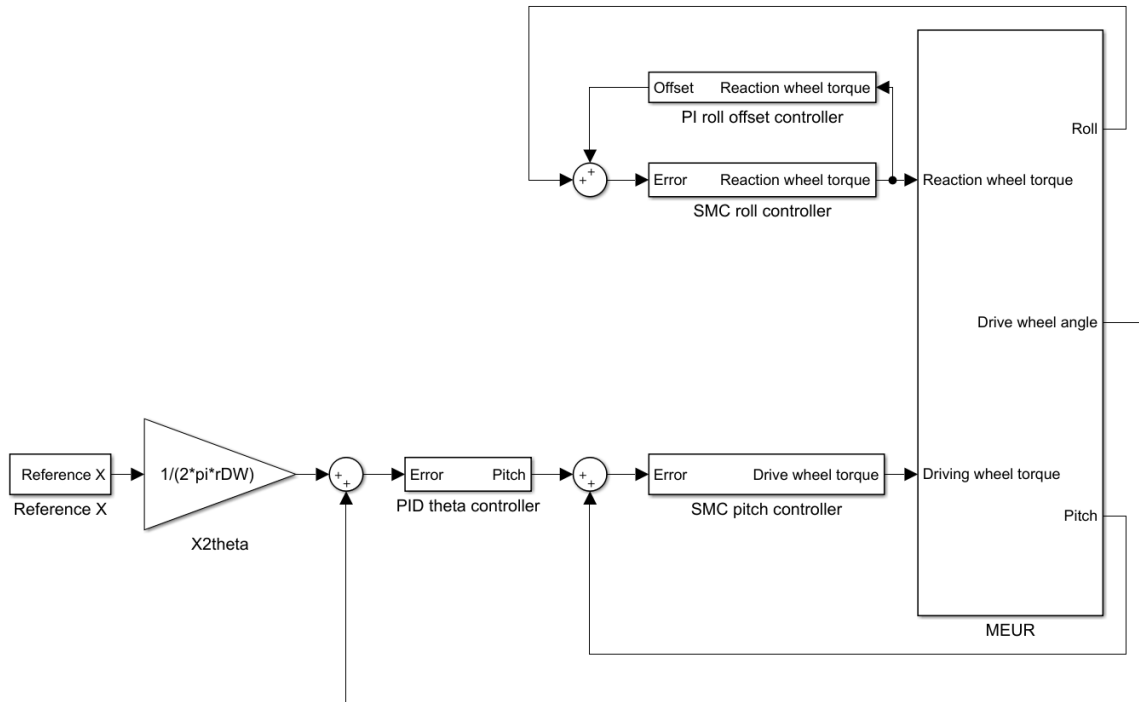


Figure 2.6: Controller MEUR as designed by De Vries [3]

For the lateral or roll direction a Sliding Mode Controller (SMC) is used with a Proportional and Integral controller (PI) for offset compensation. The output of the SMC is calculated with:

$$u = \rho \frac{\sigma}{|\sigma| + \epsilon} + k_v \dot{e} + k_p e \quad (2.1)$$

Where

$$\sigma = \dot{e} + m e \quad (2.2)$$

$$k_v = 2m, k_p = m^2, m = \omega_c \quad (2.3)$$

In these equations e is the error signal and \dot{e} the velocity error signal. ρ is the amplitude, σ the sliding mode manifold and ϵ a smoothing parameter. k_v is a derivative term in the control law and k_p a proportional. The parameter m set the bandwidth of the controller and is set to the crossover frequency ω_c .

The parameters for the roll SMC are listed in table 2.1. The PI is needed to compensate for offset due to what is defined as zero does not need to be the exact upright position. Without this controller the SMC would try to keep the offset and the reaction wheel will spin up until it reaches its maximum velocity at which it cannot exchange any more torque and the MEUR will topple over. The parameters for the PI are found in table 2.2. The PI also has a built-in second order low-pass filter set at $1Hz$.

The longitudinal or pitch direction uses again a SMC for the pitch with a cascaded Proportional, Integral and Derivative controller (PID) for θ which is linked by the no slip condition to the X position. The parameters for the SMC are stated in table 2.3 and for the PID in table 2.4. It should be noted that the longitudinal SMC uses a different formula for k_v , namely $k_v = m/5$.

Parameter	Value
ω_c	12rad/s
ρ	1Nm
ϵ	0.1rad/s

Table 2.1: Parameters SMC roll

Parameter	Value
ω_c	5rad/s
ρ	0.3Nm
ϵ	0.1rad/s

Table 2.3: Parameters SMC pitch

Parameter	Value
k_p	$1^\circ/\text{Nm} \approx 0.0175\text{rad}/\text{Nm}$
k_i	$0.25^\circ/(\text{Nm} \cdot \text{s}) \approx 0.0044\text{rad}/(\text{Nm} \cdot \text{s})$

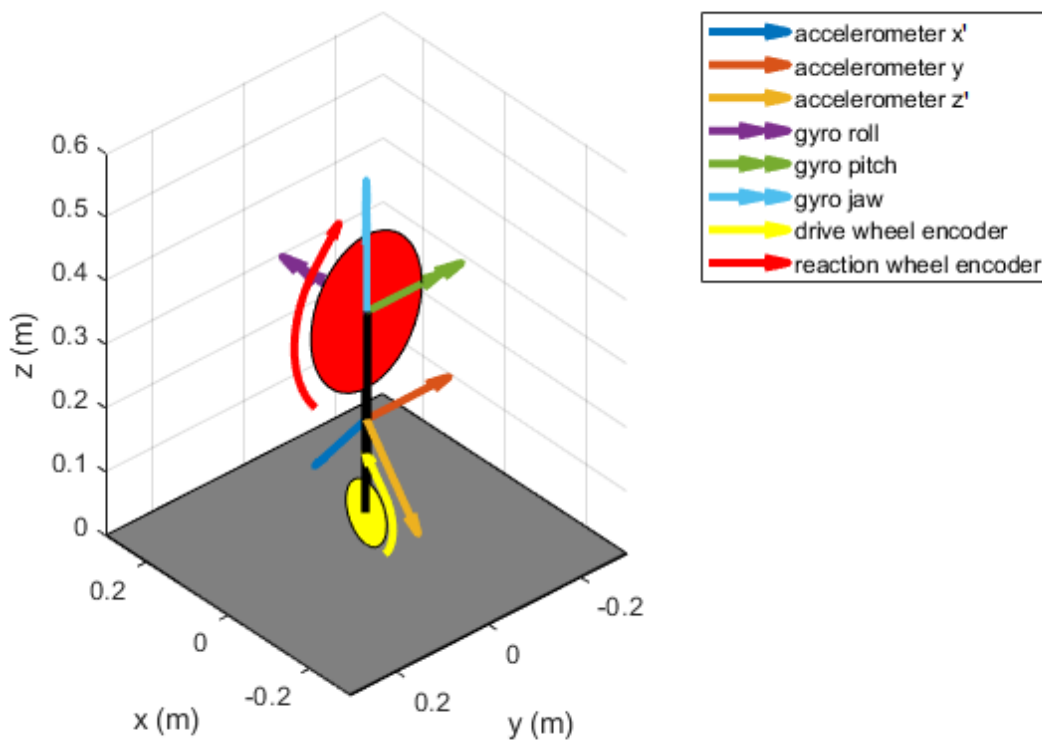
Table 2.2: Parameters PI roll offset

Parameter	Value
k_p	$0.015\text{rad}/\text{rad}$
k_i	$0.01\text{rad}/(\text{rad} \cdot \text{s})$
k_d	$0.002\text{rad} \cdot \text{s}/\text{rad}$

Table 2.4: Parameters PID θ

2.3 Sensor setup

The MEUR has the the following sensors; a three axis accelerometer; three single axis gyros; two motor encoders. In figure 2.7 the orientation of these sensors are schematically represented. De Vries chosen to rotate the accelerometer with an angle of 45° around the Y axis. From the previous section it can be concluded that the following signals are needed for controller: roll, roll velocity, pitch, pitch velocity, driving wheel angle and driving wheel velocity.

**Figure 2.7:** Sensor orientations

How the sensor inputs can be converted to the needed signals is explained in detail in the thesis report of De Vries [3, Chapter 3] for the position signals. For the conversion an extra signal is needed, namely the driving wheel acceleration. The conversion uses a complementary filter with the accelerometer measuring gravity for the low frequencies and the gyros for the high frequencies.

The report of De Vries is lacking elaboration on how the velocities and newly needed acceleration signals are constructed, therefore this will be elaborated here. This is needed because later on in this report some parts of the setup will be changed. The roll velocity signal was constructed by a hard differentiator from the roll position signal followed by a second order low-pass filter set at $15Hz$, as is illustrated in figure 2.8. For the pitch velocity signal this was done by filtering the gyro signal first with a second order high-pass filter set at $0.5Hz$ and then a second order low-pass filter of $15Hz$, see figure 2.9. The driving wheel velocity and acceleration signals were constructed by use of a state variable filter set at $5Hz$ from the motor encoders signals.

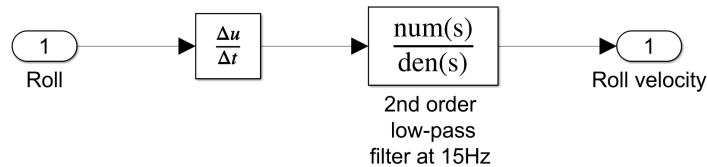


Figure 2.8: Roll velocity construction

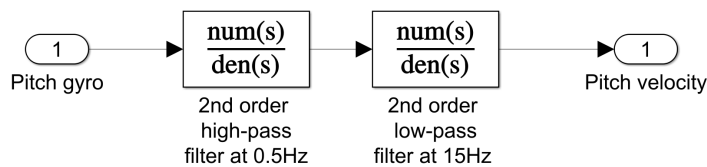


Figure 2.9: Pitch velocity construction

Simulation model

3.1 SPACAR model

Langius [6] presented a SPACAR model for a MEUR. This model was compared by Langius to his analytical derived equations of motion of the MEUR used in his work and found to be accurate. This SPACAR model was edited to use it for the experimental setup of this research, see appendix A. Extra inputs and outputs were added for simulation and control purposes.

The inertia parameters were obtained from the SolidWorks model. The damping parameters were kept the same for the back ElectroMotive Force (EMF). Although the motors are current controlled so therefore have no back EMF. But the damping is kept since there will be an unknown mechanical damping. This is due to friction. Damping was also added between the floor and the wheel in the jaw direction, this parameter is unknown but set to a damping of $0.26Nm/rad/s$. Since this will result in a time constant of approximately 0.1, which was considered to be a good starting estimation.

3.2 Model comparison to experimental setup

The model was compared visually to the experimental setup and found to behave similarly. That means that controllers which are mostly stable in a simulation are also stable in the experimental setup and vice versa. The simulations did however perform better than the experimental setup as it shows less swing. This will become clear from the comparison of simulations and experiments in chapters 5 and 6. The reason why the simulations outperformed the experimental setup is most likely due to the following differences between the model and the experimental setup:

- No sensor noise in the model
- No sensor delay in the model
- Ideal sensors in the model (sensors measure perfectly the intended coordinates, instead of calculating the intended coordinates from other signals)

From these differences the sensor delay was simulated, see figure 3.1, and it was found that the simulation showed similar behavior as the experimental setup, such as larger swings, when the velocity signals were delayed with at least $2ms$. The comparison in behavior was done by looking at the similarity between a movie of the simulation with an experiment. This was most noticeable with roll. When the pitch velocity signal was delayed similar results were visible.

The delay however is ignored in the simulations done later in this report because it creates an uncertainty when trying out new controllers for the first time. It was chosen to accept the extra swing that this delay causes when switching from simulations to experiments. However, sometimes this results in a need for slower reference profiles to prevent the MEUR from toppling over.

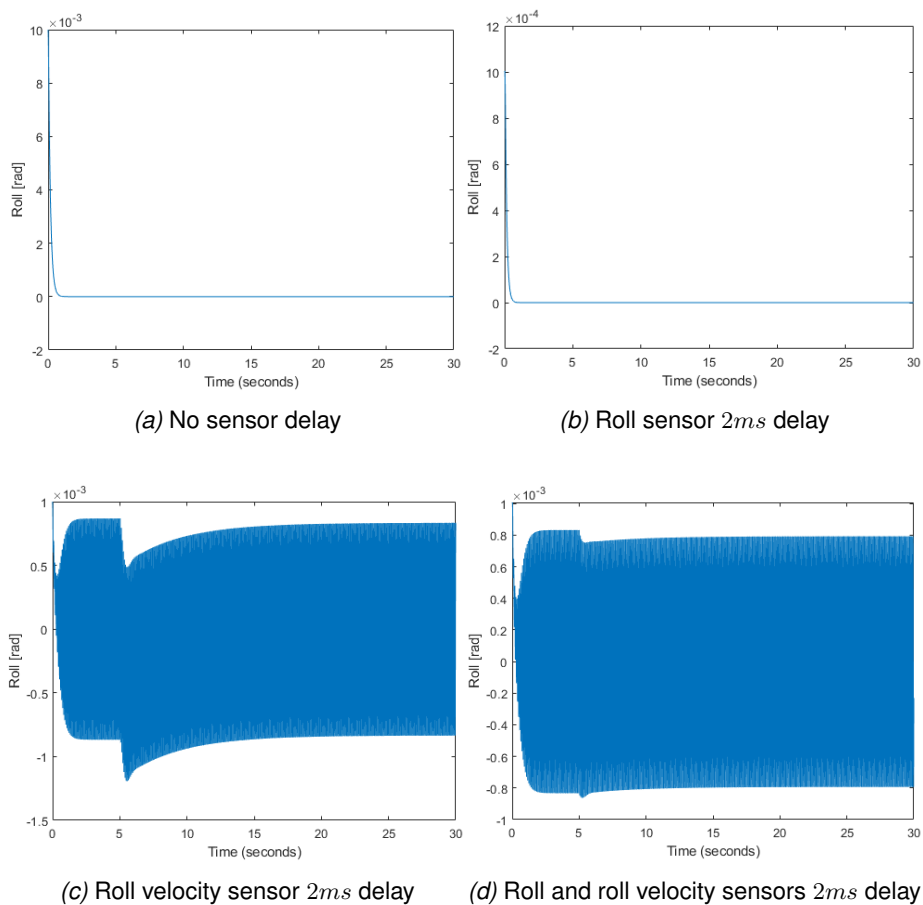


Figure 3.1: Roll delay simulations

Experimental setup

4.1 Existing setup

Prior to this research the MEUR of the SDAC research group was controlled from a desktop PC equipped with a *National Instruments PCI-6221* interface card and running a Simulink Realtime application. This setup showed a problem due to the need for a wire between the PC and the MEUR for the sensor and control signals. Since one of the goals of this thesis is the adding of cornering or turning the wire can give problems due to its unpredictable mass and stiffness.

4.2 New Setup

To eliminate the wire, the MEUR should be controlled with an on-board controller that operates standalone and/or wireless. There are multiple ways to get this done. To select the most suited method the wishes and requirements were drafted. Appendix B explains how the wishes and requirements were drawn up. It also elaborates on the design choices and design process. A summary of the requirements and wishes is given in table 4.1.

After the MEUR was made wireless with the designed board [7], the existing controllers were tested for showing similar system behavior. This was not the case. After the sensor setup was slightly adjusted and the controllers re-tuned, the MEUR was able to remain upright and follow a reference. In the next paragraph the adjustment to the sensor setup is addressed and the re-tuning of the controller in the paragraph after that.

The hardware of the sensor setup was altered by changing the power supply of the analog sensors. This was done by switching from the 5V output from the Escon 50/5 motor controller to a balanced power supply. Because it was noticed that when the motor controller was driving the motor the voltage of the output would fluctuate. This is unwanted because the offset and sensitivity of the analog sensors are directly related to their power supply voltage. Thus this leads to improper measurements. After switching to the balanced power supply and a new calibration the software part of the sensor setup was altered. The roll and pitch velocities use their gyro signals directly. So the setup does not use a hard differentiator anymore, eliminating noise problems. Also less filters are needed thus less calculations.

Parameter	Requirement	Wish
Interconnectivity	Results importable in Matlab	Run in Simulink
Control and measurements	Standalone	Real-time wireless
Sample frequency	1kHz	10kHz
Number of analog inputs	6	8
Analog input range	$\pm 10V$	setable to lower range to get higher resolution
Analog input resolution	0.625mV	setable to lower
Number of encoder inputs	2	3
Encoder range	$\pm 203719counts$	$\pm 2^{31}counts$
Number of analog outputs	2	3
Analog output range	$\pm 10V$	-
Analog output resolution	5mV	0.625mV

Table 4.1: Wishes and requirements

The re-tuning of the controllers lead to the parameters found in table 4.2. The other controllers were kept as they were. The reason why the retuning was necessary is difficult to test. It is expected this is due to a less computational powerful platform for the controller being used. The powerful desktop PC was switched for a *Raspberry Pi 3B*. This can result in an increased output calculation time. Therefore, the system is not acting as discrete as it did before. This is further clarified with figure 4.1 where a single time step is displayed as it could be in the old and new setup.

Parameter	Value
ω_c	10rad/s
ρ	1Nm
ϵ	0.1rad/s

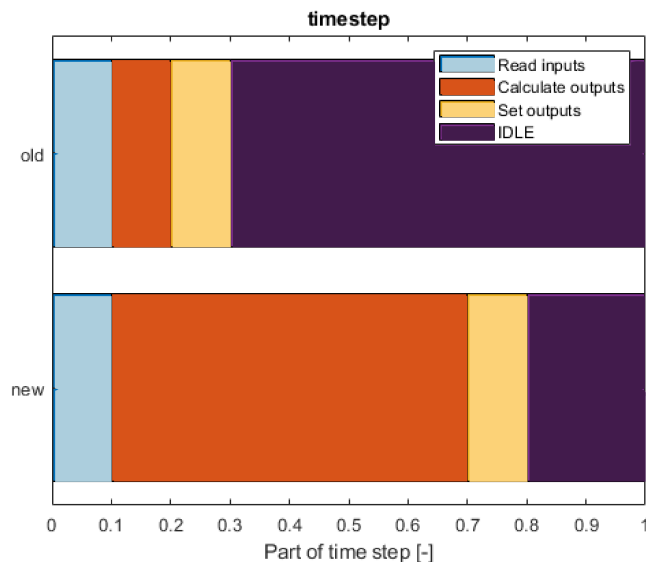


Table 4.2: Parameters SMC roll

Figure 4.1: Example of a single time step, between a desktop PC (old) and a *Raspberry Pi 3B*(new)

Improved longitudinal tracking

As stated in section 1.1 it would be favorable for the MEUR to get better tracking to get the MEUR more suited for its role as a delivery drone, since it will become a better controllable drone. Feedforward is one of the most powerful tools to get better tracking. Therefore, it was investigated if it is applicable to the MEUR in the longitudinal direction also known as the drive direction.

It was chosen to add the feedforward controller parallel to the θ PID as illustrated in figure 5.1. Signals can be position signals and/or its derivatives which are not shown separately to retain readability. The reason to add the feedforward controller parallel to the θ PID is to assure the system will prioritize not toppling over above following the reference. The feedforward controller is of the acceleration feedforward type, which will be outlined in the next section.

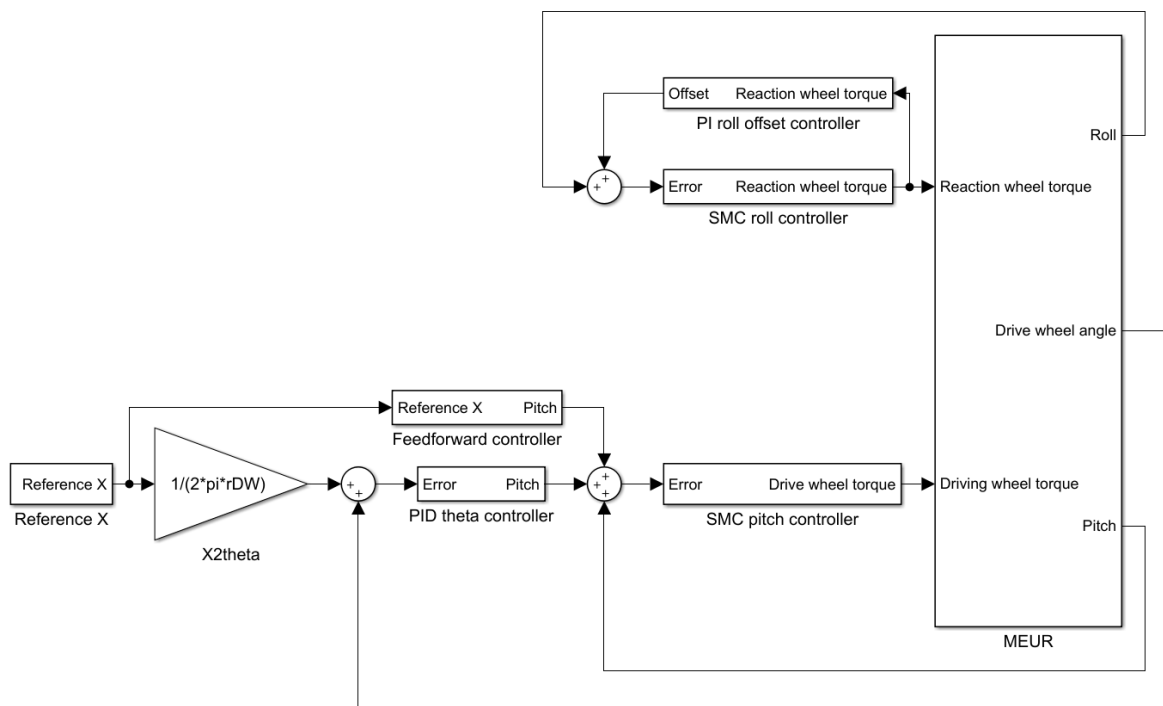


Figure 5.1: System with feedforward

5.1 Derivation

From figure 5.1 it follows that the feedforward needs to be a function of the reference position to a pitch angle. The derivation of this function was done from the free body diagram in figure 5.2.

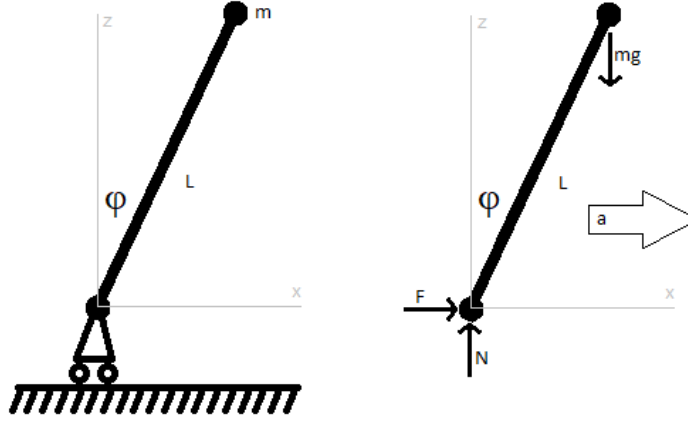


Figure 5.2: Free body diagram longitudinal system

To get a certain constant acceleration a it follows that driving force F is equal to ma . For the constant acceleration a the MEUR should remain in the same configuration, thus ϕ should be constant. From the angular equation of motion:

$$L \cdot N \cdot \sin \phi - L \cdot F \cos \phi = L \cdot m \cdot g \cdot \sin \phi - L \cdot m \cdot a \cdot \cos \phi = \ddot{\phi} \cdot J_p \quad (5.1)$$

The feedforward equation can be derived for a steady pitch angle ϕ , hence $\ddot{\phi} = 0$:

$$\phi = \arctan \frac{a}{g} \quad (5.2)$$

Because the acceleration of the reference is known, this equation is the feedforward function. Since the feedforward function does not depend on any model parameters it has a high certainty factor thus it is set at 1, although its derivation is only valid for a constant acceleration.

5.2 Validation with simulations

To check if the proposed feedforward will give better tracking two simulations were run. One without the feedforward and one with. It was chosen to use a skew-sine starting at $10s$ with $t_m = 4s$ and $h_m = 0.5m$ for the simulations. The reference profile is displayed in figure 5.3. The results of these simulations are displayed in figure 5.4. From the simulations it is clear the tracking is indeed better. It is also clear that the feedforward does not eliminate the feedback controller. This is mostly due to the underactuated nature of the system. To get a certain pitch angle needed for the wanted acceleration, the drive wheel must first drive away from its reference position thus creating an error.

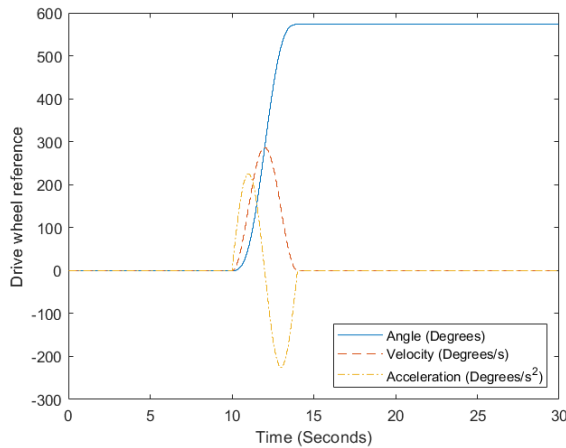


Figure 5.3: Drive wheel skew-sine reference

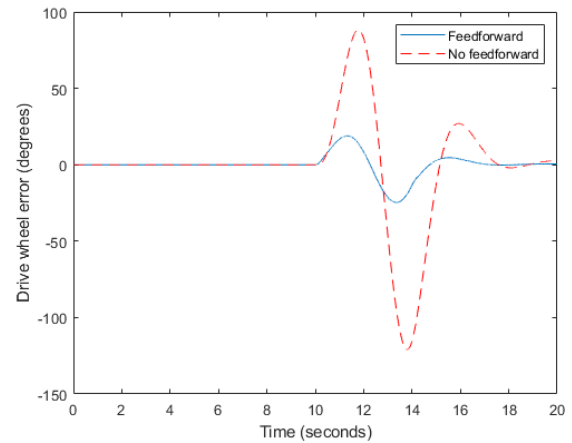


Figure 5.4: Simulations with skew-sine reference

Also the assumption of $\ddot{\phi} = 0$ plays a small part in not eliminating the feedback controller. Which is shown by switching the reference to a second order profile which has a constant acceleration, see figure 5.5. Thus if the assumption plays a major role the error of this simulation should be significantly smaller. Although the error is smaller which is clear from figure 5.6 it is not as significant compared to the underactuated effect. Also the simulation with the second order reference is not as smooth as the skew-sine reference simulation. Which can be expected since the feedforward controller will give a discontinuous signal since the acceleration profile is not continuous thus it wants the pitch to jump. Which is of course not possible.

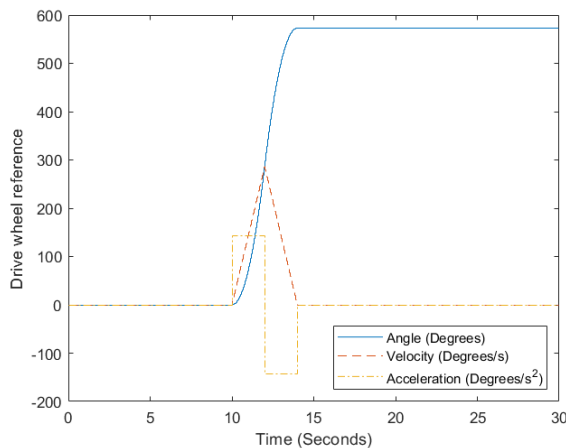


Figure 5.5: Drive wheel second order reference

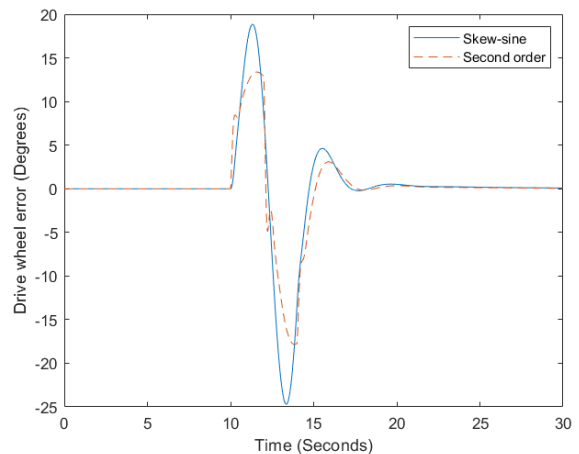


Figure 5.6: Simulations with both references

5.3 Experimental validation

The addition of the feedforward controller was validated on the MEUR. The skew-sine reference profile, see figure 5.3, was used from the simulations. This since the smoothness is preferred over a little better tracking. Since nonsmoothness can result into a toppled MEUR due to coupling effects to the roll or existing higher order dynamics.

In figure 5.7 the results of the experiments are displayed with and without feedforward. The MEUR is released after $5s$. Since the reference starts at $10s$ the MEUR has $5s$ to stabilize and stand as stationary as it can. Because the amplitude of the swinging is not decreasing it can be expected that the MEUR is not capable of standing anymore stationary. In the experiments the advantage of the feedforward controller is not as strong as it was in the simulations due to the swinging. However, some benefit from the feedforward can be observed. As the characteristic sine curve of the error is still visible in the case without feedforward.

It should be noted that to get these results the reference was set to a displacement that the system without feedforward could follow and remain stable. For example it did not topple over in roll direction due to coupling. The system with feedforward could follow a displacement of at least twice as large in the same time and remain stable.

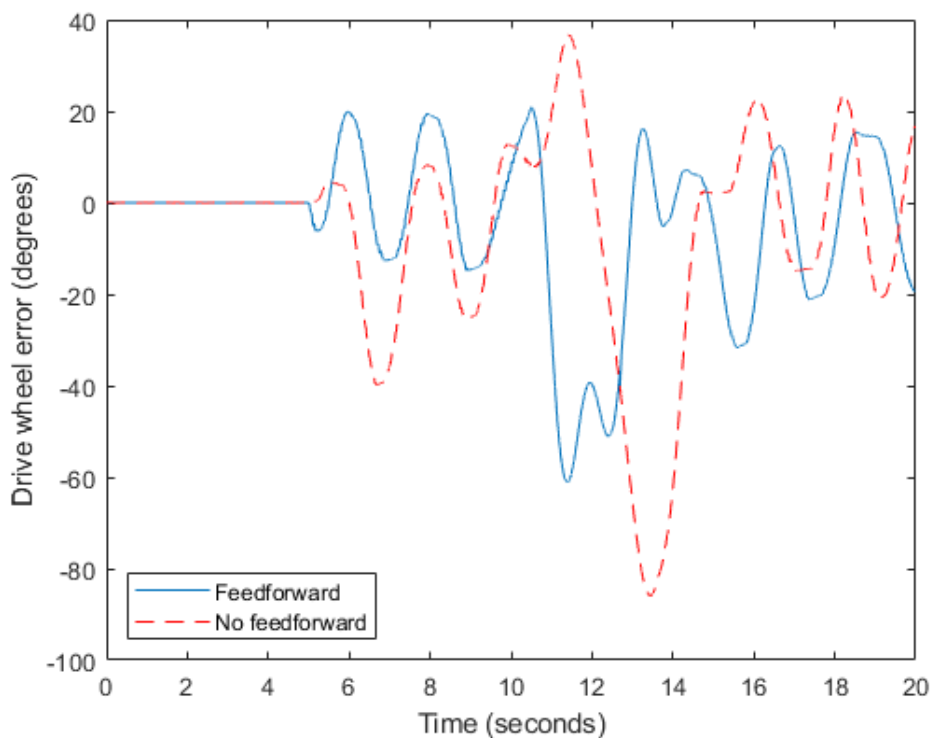


Figure 5.7: Experiments with skew-sine reference

Cornering and turning

As stated in the introduction to get the MEUR working as a delivery drone it should at least be able to either make comers or turns. The main difference between these maneuvers is that the MEUR is either moving forward or remains standing in its place, see section 1.1. Both are investigated.

6.1 Cornering

It was thought that cornering would be more straightforward to implement compared to turning since when the MEUR is in a pitched position there exists a coupling from the reaction wheel motor to the jaw, as is plotted in figure 6.1. These plots are made by using two SPACAR models, one upright and one in a pitched position. From these models the state space description were acquired.

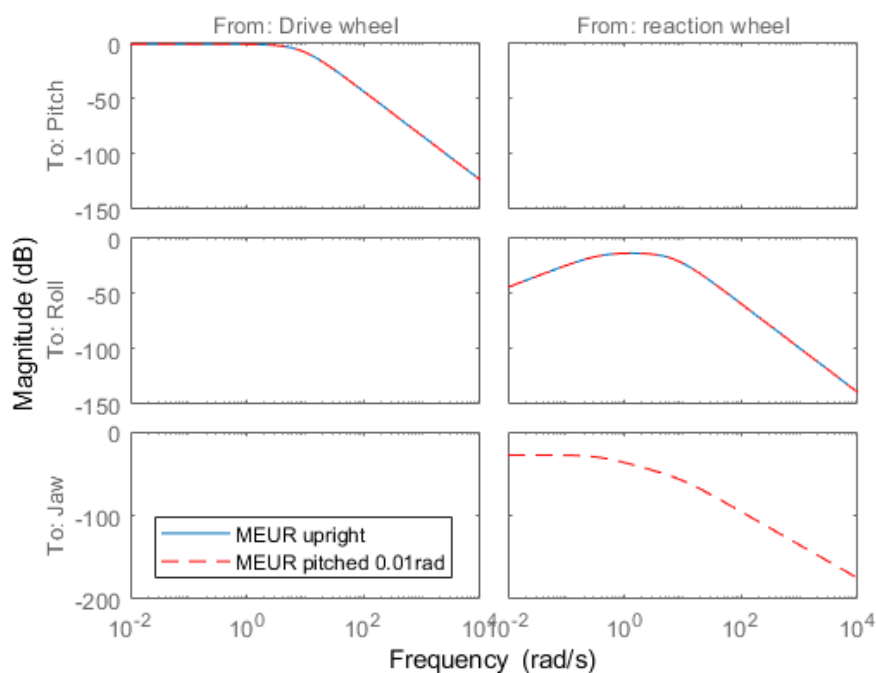


Figure 6.1: Bode magnitude plots MEUR: upright and pitched

However, after trying to implement cornering on the simulated MEUR it was noticed this was not as straightforward as was expected. Although there exist coupling from the reaction wheel motor to jaw, it is not as simple to set the MEUR to a certain roll angle while it is driving forward at constant velocity and thus pitch, due to friction. This does not result in a corner as one would instinctively expect since this works on bicycles.

In the cornering simulation the offset PI was removed, since it creates an uncertainty if either a corner is not possible or this controller opposes the corner attempt. The simulation starts by accelerating the MEUR in X for $2s$ after which it will take on a constant velocity for the rest of the simulation, which stabilizes from around $6s$. Next at $6s$ a step of -0.3° is set in the roll, which is an impulse on its velocity. The results of this simulation are shown in figure 6.2. From the simulation it can be seen that the jaw reacts to the change of the roll in an impulse response manner, but does not react to roll step.

Thus the jaw only depends on the roll velocity and not its position. Therefore, this way to make a corner will not be possible to implement since to get a certain jaw angle the roll angle needs to be able to set to a certain angle. Which can be impossible since the roll angle is limited to prevent the MEUR from toppling.

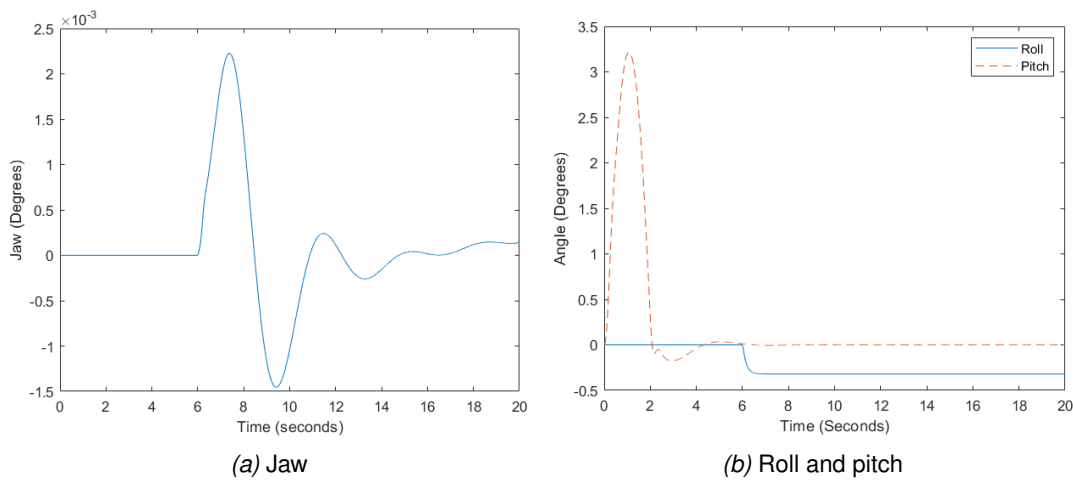


Figure 6.2: Cornering simulation

If cornering is possible there is an ideal roll angle. This angle is chosen so the reaction wheel will not have to perform work during the corner. The equation for this angle is:

$$\gamma = \arctan \frac{v^2}{g \cdot r} \quad (6.1)$$

Where v is the longitudinal velocity of the MEUR and r the radius of the corner. The derivation of this equation is given in appendix C. In theory it should not be necessary to set the MEUR to this angle due to the offset PI. However, the initial roll angle does need to be set to start the corner. Also this equation only works one way. It only states at which roll angle the MEUR should be set for a corner with a certain radius and longitudinal velocity and not the other way around, thus setting the MEUR to a certain angle and longitudinal velocity will not result into a corner with a radius r .

6.2 Turning

Because cornering is not as straightforward as was thought, as in setting a roll angle while driving forward does not result in a corner, turning was further investigated. Turning MEUR's [8] do already exist. However, these are of a slightly different type, since they have an extra actuator acting on a turntable, see figure 6.3. While this is a valid option to add turning control to a MEUR it is not preferred for a delivery drone, since it will add more mass and the placement of the package will be more difficult due to the space needed for the turntable. Thus it is preferred if turning would be possible without adjustment of the setup. Majima [9] presented a control strategy for the jaw. This strategy is based on the simplified equation of motion:

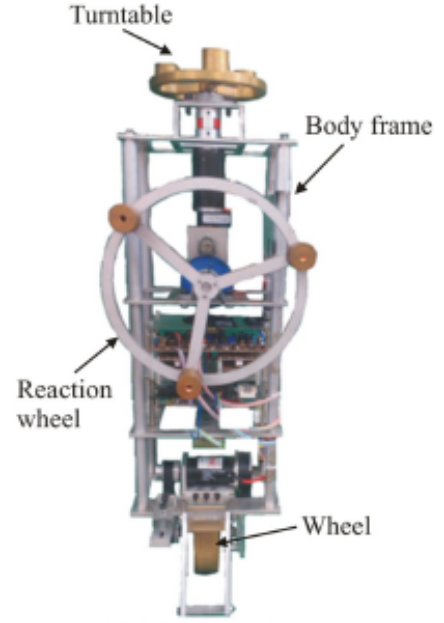


Figure 6.3: Unicycle robot [8]

$$B_{p1}\ddot{\theta} + B_{p2}\ddot{\phi} + B_{p3}\dot{\phi} + B_{p4}\phi = C_1u_p \quad (6.2a)$$

$$B_{r1}\ddot{\gamma} + B_{r2}\dot{\gamma} + B_{r3}\gamma = C_2u_r \quad (6.2b)$$

$$B_{y1}\ddot{\psi} + B_{y2}\dot{\psi} + (B_{y3}\ddot{\phi} + B_{y4}\ddot{\theta})\gamma = 0 \quad (6.2c)$$

Where all B_{\dots} and C_{\dots} are constants. Next the following is assumed:

$$\begin{aligned} \gamma &= h_1 \sin(\omega t) \\ \ddot{\theta} &= h_2 \sin(\omega t + T) \\ \ddot{\phi} &= h_3 \sin(\omega t + T) \end{aligned} \quad (6.3)$$

Where h_1 , h_2 and h_3 are yet to be chosen constants, ω the angular velocity of the sinus function and T a phase shift. Rewriting equation 6.2c with the assumptions leads to:

$$B_{y1}\ddot{\psi} + B_{y2}\dot{\psi} = -h_1(B_{y3}h_3 + B_{y4}h_2) \sin(\omega t) \sin(\omega t + T) \quad (6.4)$$

A new constant $K = h_1(B_{y3}h_3 + B_{y4}h_2)$ is introduced. Leading to:

$$\begin{aligned} &= -K \sin(\omega t) \sin(\omega t + T) \\ &= -K(\cos(T) - \cos(2\omega t + T))/2 \end{aligned} \quad (6.5)$$

Therefore, by use of the hypothetical input $u_y \equiv -K(\cos T - \cos(2\omega t + T))/2$ the jaw can be controlled. During one cycle π/ω the integrated value of this input is:

$$\bar{u}_y \equiv -K \cos(T)/2 \quad (6.6)$$

Majima implemented this strategy by using two Proportional controllers (Ps) with sinus references on both roll and pitch. Both sinus references have the same frequency but have a settable phase difference T between them. Depending on the phase difference the jaw can be controlled.

The idea of the reference was used to create a system that generates references for the roll and pitch depending on its input. In this system the phase difference between the sinuses for the pitch and roll is dependent on the sign of the input. The phase difference is either 0 or π insuring maximum jaw velocity control, as can be concluded from figure 6.4. This results in either the sinuses being completely in-phase or in counter-phase. Thus, the reference can be made from a single sinus. The amplitude of the sinuses depends on the magnitude of the input of the system that generates the reference. Therefore, the MEUR does not need to be kept in a sinus movement when the error is zero or when the error is small the movement is small. Thus, the shaking is limited.

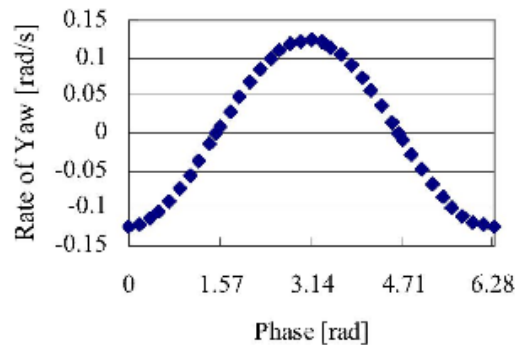


Figure 6.4: Change rate of jaw with phase difference as presented by Majima [9]

In figure 6.5 a schematic view of the controller is given with the added jaw Single input Multiple output (system) (SiMo) and a PD to control this system.

In figure 6.6 the jaw SiMo is shown. First the input is limited from -5° to 5° to limit the amplitude of the sinus reference. The sinus running at $20rad/s$ is generated internally in the system. This frequency was chosen based on a few simulation so the system is fast enough to follow a jaw reference but is as low as possible to limit the shaking of the MEUR and limit the controller forces.

6.2.1 Simulated jaw plant identification

The jaw PD controls a yet unknown plant H . Since it is known a constant input leads to a constant jaw velocity the plant can be seen as an integrator. First the PD is tuned iteratively to:

$$PD_{jaw}(s) = k_p + k_d \cdot s = 1 + 0.06 \cdot s \quad (6.7)$$

It should be mentioned that the jaw is in degrees and not in radians. The PD was used to follow a line reference of $h_m = 90^\circ$ and $t_m = 6s$ starting at $10s$, see figure 6.7. The linear

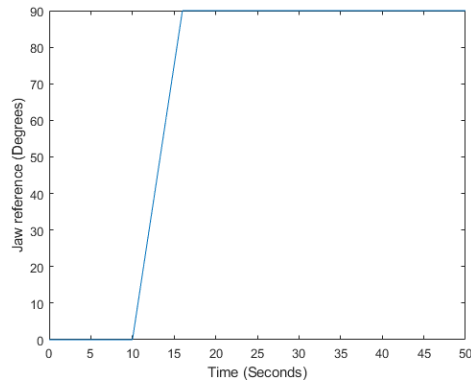


Figure 6.7: Reference jaw

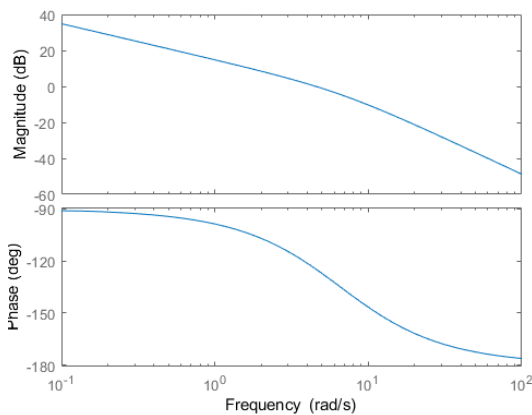


Figure 6.8: Identified jaw plant from simulation

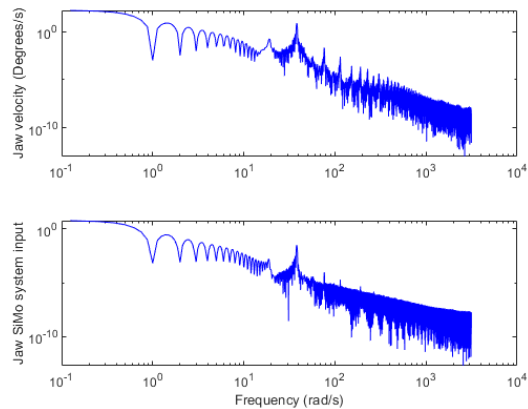


Figure 6.9: Data spectrum identification from simulation

It is verified if the plant is linear by running several identifications with different reference signals thus having different jaw velocities. If the plant is linear the identified plant should not differ. In all these identifications the h_m is kept at 90° starting at $10s$. The t_m is varied between the identifications using the following values $4s$, $6s$, $12s$ and $24s$. In figure 6.10 the differed reference signals are plotted. Non of the simulation activates the saturation. The bode plots of the identified plants are displayed in figure 6.11 and from it can be concluded that the plant is close to linear because the plots are close to each other.

6.2.2 Simulated jaw PD stability check

The iteratively tuned PD was checked for stability on the identified plant. The closed loop system was checked for right half plane poles. From figure 6.12 it is clear there are none, thus the system is stable. From the bode plot in figure 6.13 the same conclusion can be drawn. Since there is gain and phase margin. That the system is stable was expected since the PD was tuned to be stable. Now that the plant is known the PD could be optimized. This was not done since it preformed adequate for this research.

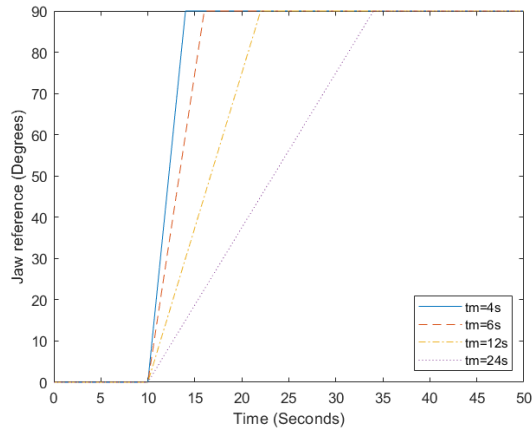


Figure 6.10: References jaw

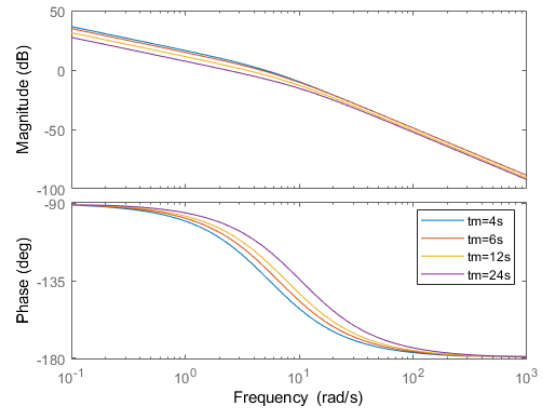


Figure 6.11: Identified jaw plants from simulations

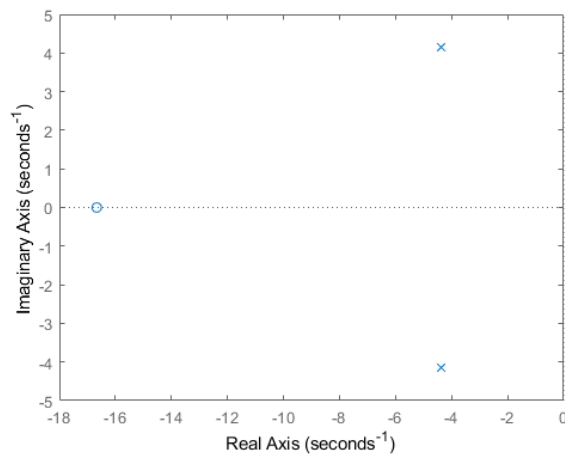
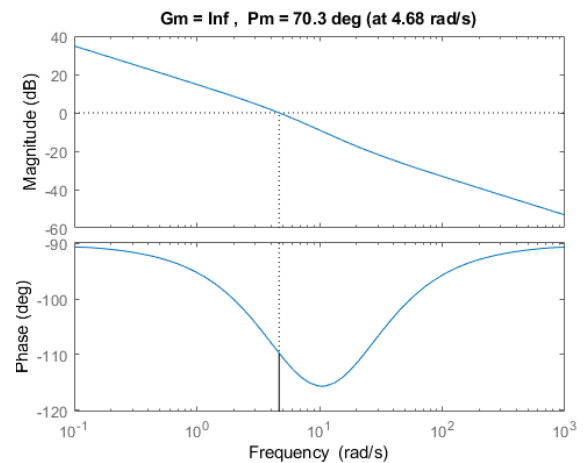


Figure 6.12: Zero pole map of the simulated closed-loop system

Figure 6.13: Bode plot simulated $C \cdot H$

6.2.3 Simulation

In figures 6.14, 6.15 and 6.16 the jaw with the reference, roll and pitch are plotted respectively of the simulation with t_m set at $6s$. The input signal of the SiMo is shown in figure 6.17. From the plots it is clear the MEUR is able to follow the reference with a small delay and also that the saturation is not activated.

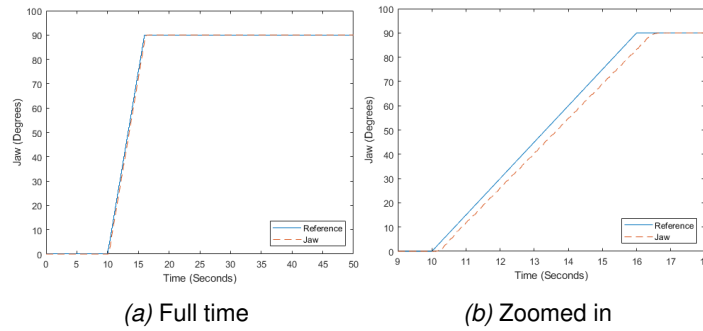


Figure 6.14: Jaw and its reference from simulation with jaw controller

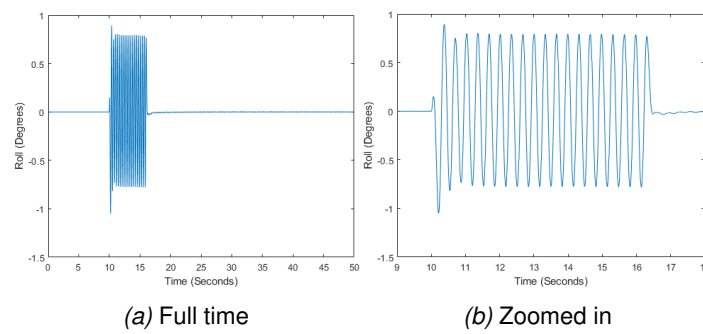


Figure 6.15: Roll from simulation with jaw controller

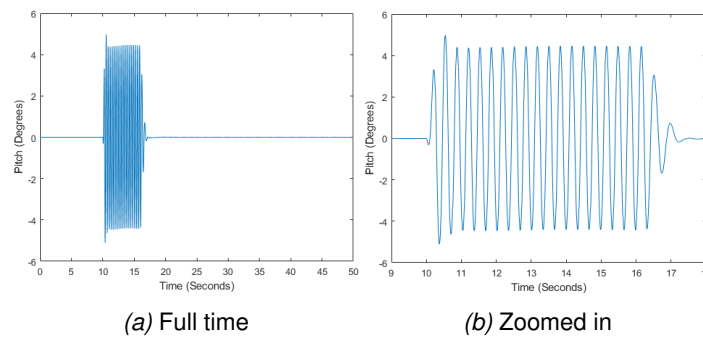


Figure 6.16: Pitch from simulation with jaw controller

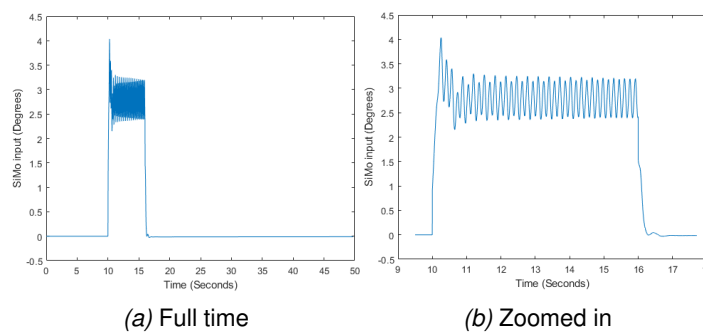


Figure 6.17: SiMo input from simulation with jaw controller

6.2.4 Experiments

Next the jaw controller was tested on the experimental setup. Straightaway it was clear the saturation of $|5^\circ|$ was too large for the setup causing the MEUR to topple over. After a few iterations trying different values the new saturation was set to $|2^\circ|$ which is the highest possible without toppling over most of the time.

Since the simulated input signal is higher the $|2^\circ|$, as can be seen in figure 6.17, it is expected that the MEUR will not be able to follow the reference. From an experiment this is confirmed, as can be seen in figure 6.18. As expected the SiMo input is saturated during the turn, see figure 6.21.

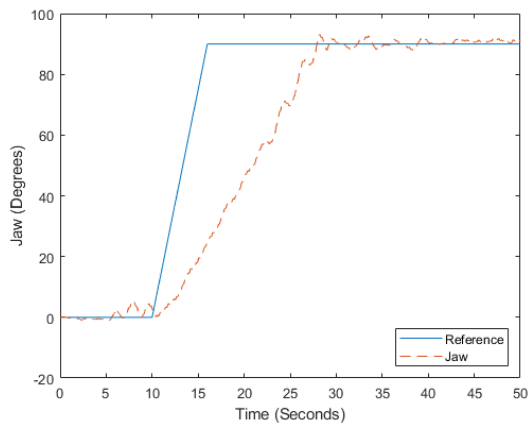


Figure 6.18: Jaw from first experiment with jaw controller

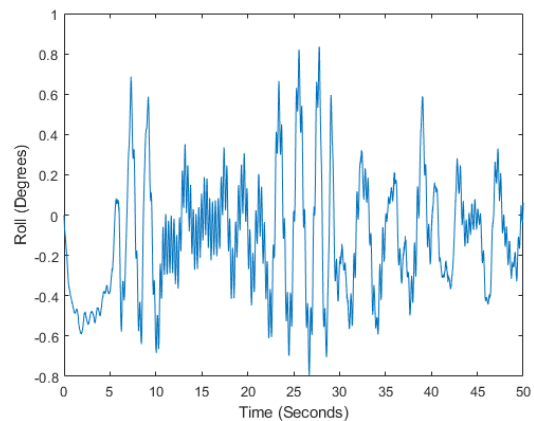


Figure 6.19: Roll from first experiment with jaw controller

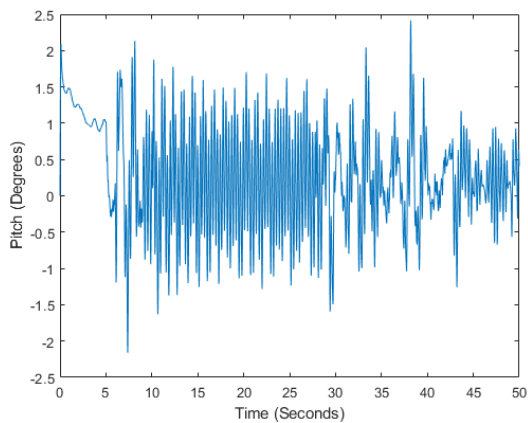


Figure 6.20: Pitch from first experiment with jaw controller

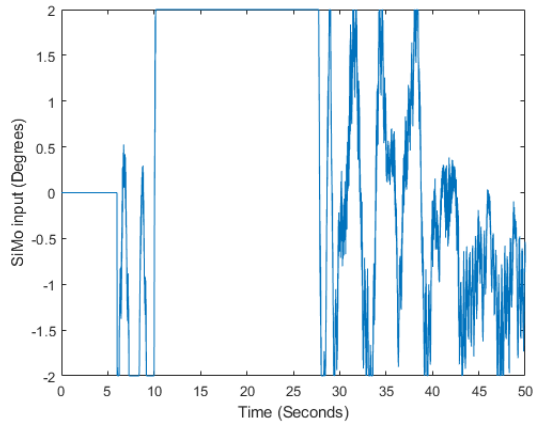


Figure 6.21: SiMo input from first experiment with jaw controller

Thus a slower reference should be used. From the experiment it can be concluded that if the t_m is at least $10s$ longer the reference should be able to be followed. Therefore, t_m is set to $30s$ and the experiment was run again. The result of which are displayed in figures 6.22, 6.23, 6.24 and 6.25.

From 6.22 it can be seen that the reference can be followed more closely but is not as straight as it was with the first experiment. It is expected that this is due to the friction. When the input of the SiMo is low the force on the jaw can become low and thus the static friction is not overcome, causing the MEUR to lag more behind its reference. This lag will lead to a higher input on the SiMo which will result in the MEUR overcoming the static friction and accelerating in jaw.

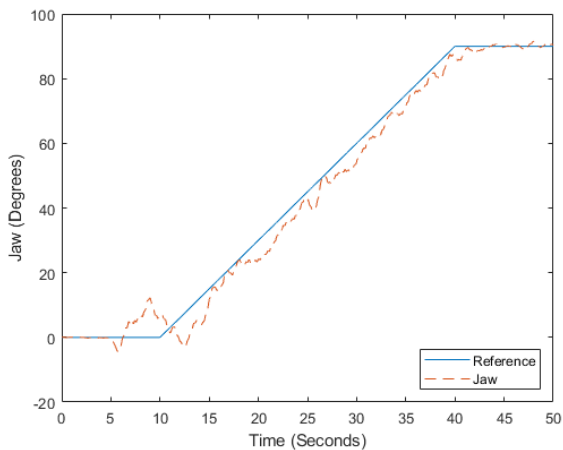


Figure 6.22: Jaw from second experiment with jaw controller

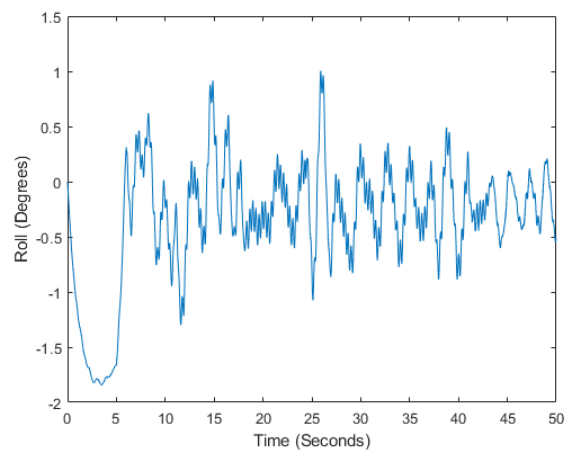


Figure 6.23: Roll from second experiment with jaw controller

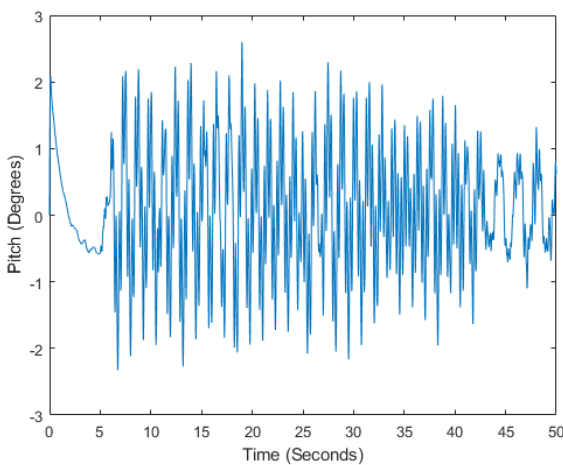


Figure 6.24: Pitch from second experiment with jaw controller

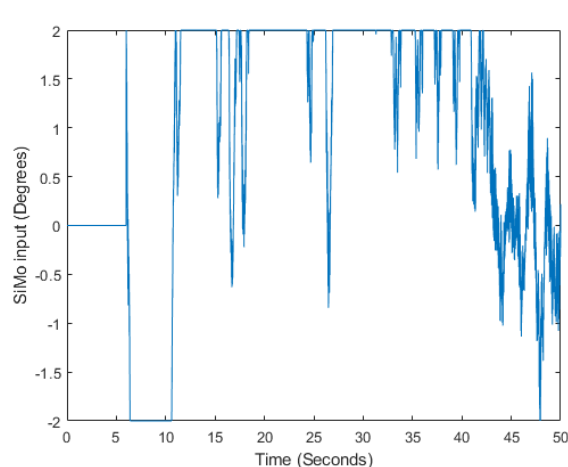


Figure 6.25: SiMo input from second experiment with jaw controller

6.2.5 Experimental jaw plant identification

From the second experiment the plant H_{exp} is identified with the same method used in 6.2.1 and compared to the identified simulated plant with the same reference with $t_m = 30s$. From this, see figure 6.26, it can be seen that the plant from the experiment is a close match to

the simulation. The transfer function of the experimental identified plant H_{exp} is:

$$H_{exp}(s) = \frac{23.94}{s^2 + 17.14s} \quad (6.9)$$

Because the plants are a close match, the SPACAR model of appendix A is not altered to another floor friction coefficient, since the damping parameter was an assumption. If the plants were not a close match it would be necessary to alter the floor friction coefficient get a more accurate model and thus more exact simulations.

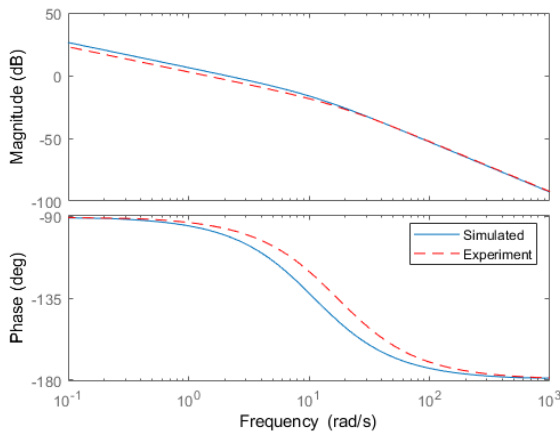


Figure 6.26: Identified jaw plant from experiment

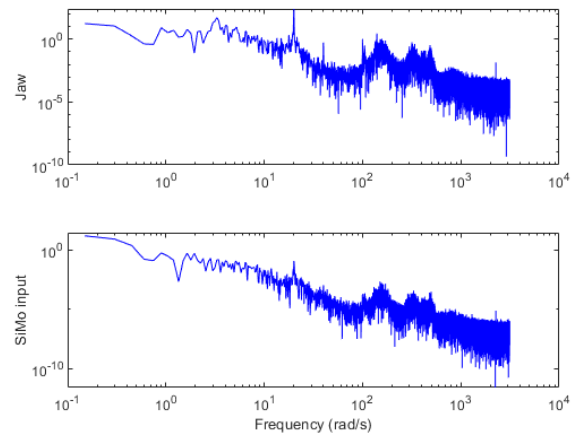


Figure 6.27: Data spectrum identification from experiment

6.2.6 Jaw PD stability check experimental setup

Since the plants H and H_{exp} differ the stability should be checked to the experimental identified plant. From figures 6.28 and 6.29 it is clear the system is stable, since there are no right half sides poles and both gain and phase margin.

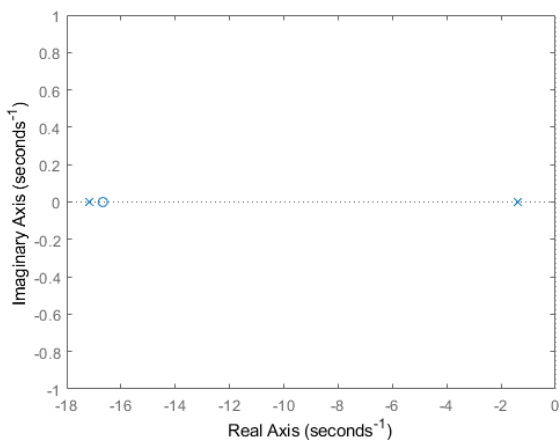


Figure 6.28: Zero pole map of the experimental closed-loop system

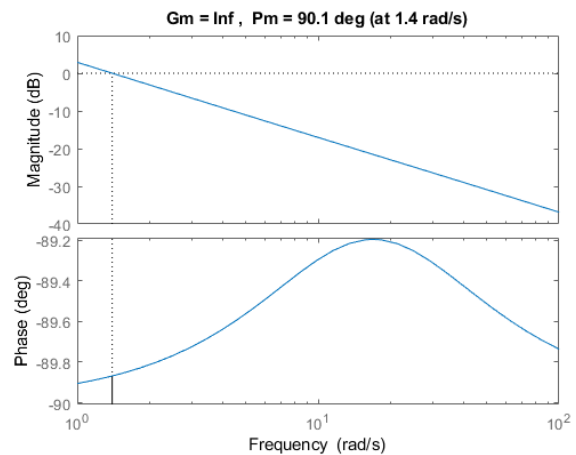


Figure 6.29: Bode plot experimental $C \cdot H_{exp}$

6.3 Reflection

In this chapter it is shown that turning is possible by implementing Majima control strategy. Cornering however is not yet proven either possible or impossible, only that a certain implementation will not work. It is possible that coupled motion is feasible with turning and driving. If this is the case then a corner could be made.

For the implementation of the turning action some parts were not optimized like the frequency of the sinus of the jaw SiMo and the parameters of the PD. When this is done the MEUR could perform even better and thus is even more suited for its role as delivery drone. Also the SiMo sets the same amplitude sinus on the roll and pitch, it is not looked into using a different gain on them. If this is done this could result in a faster turning drone since it could be possible to set a gain higher, for instance on the pitch without risking toppling the MEUR over due to more leeway on the pitch than on the roll.

Conclusions and recommendations

7.1 Conclusions

In the following sections conclusions are drawn from the results and the answers given on the research questions. Also assumptions and claims are addressed for verification.

7.1.1 Model comparison to experimental setup

The claim in section 3.2 that the simulations behave similar but outperform the experiments can be verified by comparing figures 5.4 and 5.7, figures 6.14 and 6.18, figures 6.15 and 6.19, figures 6.16 and 6.20 and figures 6.17 and 6.21. All the cases both the simulation and the corresponding experiment showed the same behavior. However, the swinging of the MEUR is a lot lower in the simulation than in the experiments.

7.1.2 Experimental setup

The designed new hardware interface board appeared to be perfectly suited for this work. Since it was as simple to use as making a Simulink model and running it. Also its performance was as expected. It could run the complex Simulink models at $1kHz$ without problems.

7.1.3 Improved longitudinal tracking

From chapter 5 it can be concluded that it is possible to add the acceleration feedforward to the MEUR and that it does improve the longitudinal tracking. This conclusion can be drawn from both the simulation, see figure 5.4, and the experiment, see figure 5.7.

7.1.4 Cornering and turning

The research question "*Can the MEUR perform corners? And how?*" can not be answered at this point. This is because it was not proven that it is possible or impossible. Only an

implementation which is not possible was looked at. Thus this question requires more investigation. This will be addressed in the recommendations.

It is shown in section 6.2 that turning of the MEUR is possible by setting two sinuses with a phase difference on both the roll and pitch.

7.2 Recommendations

From the conclusions and several observations made during the experiments the following recommendations for future research are made. These recommendations will be addressed in more detail in the coming subsections.

1. Replace the roll and pitch SMC by a different controller
2. Investigate the influence of the sinus frequency of the jaw SiMo
3. Investigate the influence of different gains of the SiMo on the roll and pitch
4. Optimize the jaw PD
5. Design and construct a new MEUR
6. Investigate a coupled movement with longitudinal movement and turning
7. Design an extra outer loop controller to navigate and control the MEUR through the real world

7.2.1 Replace the roll and pitch SMC by a different controller

It was found that during some experiments the MEUR made a high pitch sound and in measurement it was clear that the MEUR was oscillating at high frequency, see figure 7.1. It is expected the oscillating behavior is a result of the use of the SMC since it can be prone to chattering, which is high frequency switching between modes.

Also if the MEUR would be better at following a roll and pitch reference the turning could be improved, since the coupled motions would be more in sync and larger angles can be used. Resulting in higher and more accurate jaw velocities.

Switching to a classic PD or a super twisting SMC [10] chattering will no longer be a problem, since the control signal is again smooth. If the classic PD is chosen it should not have an integrating action, so it should not be a PID, since this would try to compensate the offset corrections.

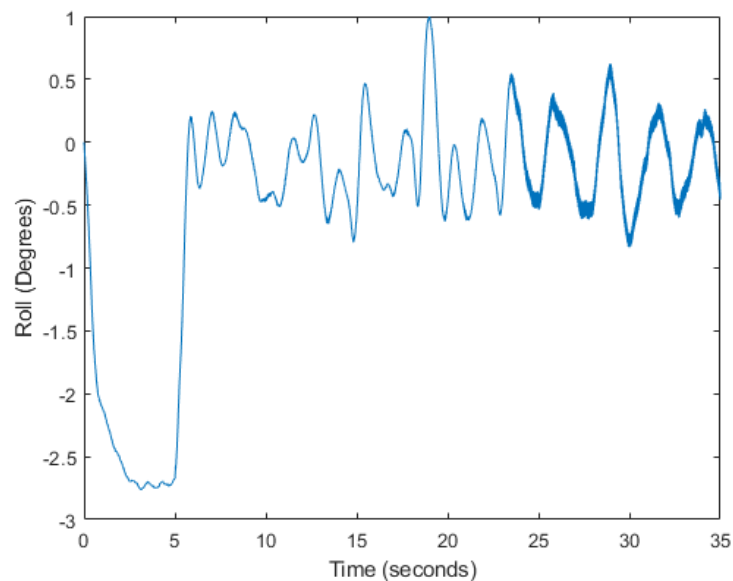


Figure 7.1: Chattering from $t \approx 23s$ onward on the roll

7.2.2 Investigate the influence of the sinus frequency of the jaw SiMo

The SiMo uses an in-phase or counter-phase sinus on the roll and pitch to get the MEUR to turn. The frequency of this sinus was based on some simulations. However, the chosen frequency may not be optimal. Thus it should be investigated what the influence is of this frequency on the system.

It is expected that setting the frequency higher would make the system better at following a reference at the cost of higher motor torques and vice versa. Also it is possible that if the frequency is set too low the experimental setup will not overcome its static friction and thus does nothing.

Therefore, investigation of the frequency influence is needed to get a better insight in what a good frequency is for the SiMo, with the trade-off between tracking and low motor torques.

7.2.3 Investigate the influence of different gains of the SiMo on the roll and pitch

Using different gains on the roll and pitch from the SiMo could result in a faster turning MEUR. This is due it is possible that there is more leeway in either the roll or the pitch than the other, thus a larger gain could be set on it.

7.2.4 Optimize the jaw PD

The jaw PD was iterate tuned since the plant was unknown. However, the plant was identified later on. Thus since the plant is now known the PD could be optimized.

7.2.5 Design and construct a new MEUR

The current MEUR from the SDAC research group was never designed to be able to turn. The fact that it is able to do so is a coincidence. Since the MEUR is at its limits during turning experiments, a lot of the turn experiments fail to 'overcurrent error' from the roll motor controller. Thus with a redesign of the MEUR either the MEUR should have a smaller mass or more powerful motors or both. Currently the MEUR uses direct drive motors [11] followed by a reduction, either by a gearbox or a belt transmission. This is not an optimal design. The direct drive motors are really good at direct drive applications delivering high torques without gearbox backlash. However, they are not the optimal choice when a gearbox is used, since they are heavy in view of torque and power delivered.

For example the roll motor and its gearbox have a mass of $m_t = m_m + m_g = 0.6kg + 0.77kg = 1.37kg$ [11], [12]. And a much more powerful DC motor and gearbox would have a mass of $m_t = 0.48kg + 0.36kg = 0.84kg$ [13], [14]. This is a significant reduction of mass while also getting more power. The direct drive motors are $90W$ [11] and the DC motors are $150W$ [13]. The example should not be used for the motor choice directly since it is possible that an even more powerful motor is desired in the redesign depending for instance on the mass of the package the MEUR needs to be able to transport in its role as a delivery drone. The motor choice is left to the designer.

The inertia of the reaction wheel should also be evaluated in the redesign. From the derivation done in appendix D it is concluded that the inertia of reaction wheel is too small and thus should be increased. This can be done by either increasing the reaction wheel mass or its radius or both. Increasing both is the most efficient.

Adding an automatic retractable landing gear would make the experiments easier since starting conditions would be more consistent compared to releasing it by hand. Also an automatic experiments stop could be added in case of an error, like too large roll and pitch angles, freeing the operator for other tasks, like observing.

7.2.6 Investigate a coupled movement with longitudinal movement and turning

Although it is not necessary for the MEUR to preform coupled motion to do its job as a delivery drone, it would become more efficient at it. Also it would answer the research question if cornering is possible. Since a corner is in essence a coupled motion.

It is unsure if coupled motion is possible. Because the derivation of the turning controller is only validated for an upright and not moving MEUR. Thus it is unknown what will happen.

7.2.7 Design an extra outer loop controller to navigate and control the MEUR through the real world

To use the MEUR as a delivery drone it should navigate and move through the real world. For this a new outer control loop is needed. Inputs for this controller could be GPS, cameras and radar sensors.

Bibliography

- [1] R. Giesen, T. H. Hoksbergen, A. A. Pleijsier, R. C. Swiersema, and K. Ywema, "PD control of a self-balancing Moment Exchange Unicycle Robot based on multiple theoretical models," *BSc graduation report, University of Twente*, 2016.
- [2] E. Dannenberg, "Redesign & Control of a Moment Exchange Unicycle Robot 'MEUR'," *BSc graduation report, University of Twente*, 2017.
- [3] J. F. de Vries, "Redesign & Implementation of a moment exchange unicycle," *MSc graduation report, University of Twente*, 2018.
- [4] K. Shikar, "Transwheel delivery drone concept." [Online]. Available: <https://kobishikar.wixsite.com/jaykob-shikar/transwheel>
- [5] R. J. van Dasselaaar, "Longitudinal stabilization of a monocycle by a reactionwheel on top," *BSc graduation report, University of Twente*, 2013.
- [6] S. Langius, "3D Modeling and simulation of a moment exchange unicycle robot," *MSc graduation report, University of Twente*, 2011.
- [7] F. B. Koopman, "Raspberry Pi ControlBoard (SDAC)," 2019. [Online]. Available: <https://vcs.utwente.nl/source/raspControlBoard/>
- [8] Y. Rizal, C. Ke, and M. Ho, "Point-to-Point Motion Control of a Unicycle Robot: Design, Implementation, and Validation," *Proceedings - IEEE International Conference on Robotics and Automation*, 2015.
- [9] S. Majima, T. Kasai, and T. Kadohara, "A Design of a Control Method for Changing Yaw Direction of an Underactuated Unicycle Robot," *TENCON Conference*, vol. 10, 2006.
- [10] J. van Dijk, "Motion and vibration control," *Lecture notes, University of Twente*, 2016.
- [11] Maxon Motor, "EC 90 flat 90 mm, brushless, 90 Watt," *Datasheet*, 2017. [Online]. Available: https://www.maxonmotor.com/medias/sys_master/root/8825435389982/17-EN-271.pdf
- [12] —, "Planetary Gearhead GP 52 C 52 mm, 4.030.0 Nm," *Datasheet*. [Online]. Available: https://www.maxonmotor.com/medias/sys_master/root/8831071289374/2018EN-359.pdf

- [13] —, “RE40 40 mm, Graphite Brushes, 150 Watt,” *Datasheet*. [Online]. Available: https://www.maxonmotor.com/medias/sys_master/root/8830469799966/2018EN-132.pdf
- [14] —, “Planetary Gearhead GP 42 C 42 mm, 3.015.0 Nm,” *Datasheet*. [Online]. Available: https://www.maxonmotor.com/medias/sys_master/root/8831071158302/2018EN-354.pdf
- [15] Analog-Devices, “ADXRS623,” *Datasheet*, 2010. [Online]. Available: <https://www.analog.com/media/en/technical-documentation/data-sheets/adxrs623.pdf>
- [16] —, “ADXL327,” *Datasheet*, 2009. [Online]. Available: <https://www.analog.com/media/en/technical-documentation/data-sheets/adxl327.pdf>
- [17] Maxon Motor, “MILE Encoder for EC 90 flat,” *Datasheet*, 2014. [Online]. Available: https://www.maxonmotor.com/medias/sys_master/root/8814678704158/enx-ec90flat-mile-okt-en.pdf
- [18] —, “Escon 50/5,” *Datasheet*, 2014. [Online]. Available: https://www.maxonmotorusa.com/medias/sys_master/8810873815070/409510-ESCON-50-5-Hardware-Reference-En.pdf
- [19] M. de Groot, “Choice and implementation of an on-board control platform for a moment exchange unicycle robot,” *BSc graduation report, University of Twente*, 2018.
- [20] National Instruments, “NI myRIO-1900 user guide,” *Datasheet*, 2018. [Online]. Available: www.ni.com/pdf/manuals/376047c.pdf
- [21] MathWorks, “Raspberry Pi Support from Simulink.” [Online]. Available: <https://nl.mathworks.com/hardware-support/raspberry-pi-simulink.html>
- [22] Texas Instruments, “ADS868x 16-Bit, 500-kSPS, 4- and 8-Channel, Single-Supply, SAR ADCs with Bipolar Input Ranges,” *Datasheet*, 2015. [Online]. Available: <http://www.ti.com/lit/ds/symlink/ads8688.pdf>
- [23] Analog-Devices, “AD5360,” *Datasheet*, 2008. [Online]. Available: https://www.analog.com/media/en/technical-documentation/data-sheets/ad5360_5361.pdf
- [24] Altera-Corporation, “MAX V Device Handbook,” *Datasheet*, 2011. [Online]. Available: https://www.intel.com/content/dam/www/programmable/us/en/pdfs/literature/hb/max-v/max5_handbook.pdf

SPACAR model MEUR

HINGE 1 1 2 0.0 0.0 1.0 % psi (jaw)
HINGE 2 2 3 1.0 0.0 0.0 % gamma (roll)
HINGE 3 4 5 0.0 1.0 0.0 % theta
HINGE 4 3 4 0.0 1.0 0.0 % phi (pitch)
HINGE 5 4 9 1.0 0.0 0.0 % beta
RBEAM 6 6 4 8 1.0 0.0 0.0 % body
WHEEL 7 6 5 7 0.0 1.0 0.0 % driving wheel

OUTLEVEL -1 -1

X 7 0 0 0 % wheel contact
X 6 0 0 0.0495 % wheel center
X 8 0 0 0.1165 % cog body

FIX 1

KINX 6 1 2 % kinematic coordinates
DYNE 1 1 % psi
DYNE 2 1 % gamma
DYNE 3 1 % theta
DYNE 4 1 % phi
DYNE 5 1 % beta

END

HALT

XM 6 0.184 % mw
XM 5 0.0000676269 0 0 0.0001352538 0 0.0000676269 % Jw
XM 8 3.85 % mb
XM 4 0.039827393076923 0 0 0.033127393076923 0 0.0349 % Jb

XM 9 0.0048 0 0 0 0 0 % Ji

EDAMP 3 0.000013333333333333 % back EMF motor 1

EDAMP 5 0.001776333333333333 % back EMF motor 2

EDAMP 1 0.26 % Floor friction

GRAVITY 0 0 -9.81

STARTDE 1 1 0 0 % psi

STARTDE 2 1 0 0 % gamma

STARTDE 3 1 0 0 % theta

STARTDE 4 1 0 0 % phi

STARTDE 5 1 0 0 % beta

END

HALT

INPUTS 1 3 1 % motor 1 theta

INPUTS 2 5 1 % motor 2 beta

OUTE 1 4 1 % angle phi

OUTE 2 2 1 % angle gamma

OUTE 3 1 1 % angle psi

END

HALT

END

END

New experimental setup

B.1 Wishes and requirements

Interconnectivity

A minimal requirement of the new experimental setup is that results can be imported into Matlab such that these results can be compared to the simulations. It would be even better if the setup can run in Simulink so the simulated controller can simply be copied.

Control and measurements

The setup should work without a wire connected to it. Therefore, it should either work standalone (a program is uploaded, run and the result are downloaded) or by a wireless connection. The wireless connection is preferred since it will be easier to work with. Also it will result in a safer system since it can be stopped remotely.

Sample frequency

The current controller running MEUR runs at a sample frequency of $1kHz$. Thus this setup should at least be able to run on this frequency. It would be better if this can be upscaled for other faster controllers.

Analog inputs

The MEUR currently has six analog sensors, namely 3 gyros [15] and a 3 axis accelerometer [16]. Therefore, the new setup should have at least six analog inputs. However, in the future extra sensors could be added, like for instance 2 magnetic field sensors to act as a compass, thus it is better to have eight inputs.

Although the current sensors have outputs signals in the range of $0 - 3V$ and $0 - 5V$ for the accelerometer and gyros respectively, the sensor input range should be $\pm 10V$ since this is common for analog sensors. This will keep the door open for other sensors. While it should be able to get input over the $\pm 10V$ range it would be better if this range can be set to lower

voltages with a smaller resolution.

The gyros can produce the lowest level signals. These are used to investigate the resolution needed for the analog input. It is assumed that to accurately capture the dynamics the angular velocities should be measured in steps as small as $0.05^\circ/s$. This results in a minimum resolution of:

$$r_{in} = \omega_{smallest} \cdot S_{gyro} = 0.05^\circ/s \cdot 12.5 \frac{mV}{^\circ/s} = 0.625mV \quad (B.1)$$

Where r_{in} is the resolution, $\omega_{smallest}$ the smallest angular velocity step to be measured and S_{gyro} the gyro sensitivity. Later in experiments it was checked if the assumption of measuring angular velocities in steps as small $0.05^\circ/s$ was good enough. This was done by visually comparing the jaw over a 90° rotation with the integrated jaw gyro signal. It was found that the accuracy was good enough.

Encoder inputs

The MEUR has 2 motors [11] with encoders [17] thus to measure both rotations at least 2 encoder inputs are needed. However, it could be necessary to add a motor to this setup in the future so it would be better to have at least 3 encoder inputs.

The range is set that the MEUR can move at least $2.5m$ in both directions without overflowing. This results in a range of at least:

$$U_{encoder} = \frac{\pm x}{2\pi \cdot r_{DW}} \cdot S_{encoder} = \frac{\pm 2.5m}{2\pi \cdot 0.05m} \cdot 25600 \frac{counts}{rev} \approx \pm 203719counts \quad (B.2)$$

Where $U_{encoder}$ is the encoder range, x the distance to move in both directions, r_{DW} the radius of the drive wheel and $S_{encoder}$ the number of counts per revolution of the encoder.

This range is just good enough for experiments on the MEUR. However, for the use of the MEUR as a delivery drone it should be able to drive far without overflowing. Therefore, it is best this is a very large number. It is assumed that a 32-bit signed number will be large enough. In this case it can drive without overflowing for approximately:

$$\pm x = \pm U_{encoder} \cdot \frac{2\pi \cdot r_{DW}}{S_{encoder}} = \pm 2^{31}counts \cdot \frac{2\pi \cdot 0.05m}{25600counts/rev} \approx \pm 26.35km \quad (B.3)$$

The resolution of motor angles are dependent on the number of counts per revolution of the motor and thus on the encoder input hardware and software.

Analog outputs

The setup has two motors so the new setup should have at least 2 analog outputs. However, to make the MEUR future ready it is better to have an extra output.

The motors on the MEUR are controlled by two *ESCON 50/5* motor controllers [18]. These controllers can be controlled in three ways namely by a $\pm 10V$ differential analog signal, a

$\pm 4V$ referenced to ground analog signal and digital PWM input. PWM control is not suited for this setup since the maximum PWM frequency is $5kHz$ which is very close to sample frequency thus this can give problems. The $\pm 10V$ analog signal is chosen since it will keep the door open to other motor controllers.

To fully use the 12-bit resolution of Analog to Digital Converter (ADC) from the motor controllers the analog output should have a resolution of at least:

$$r_{out} = \frac{U_{out}}{n_{integer,12}} = \frac{10V - -10V}{2^{12}} \approx 5mV \quad (B.4)$$

Where r_{out} is the analog output resolution, U_{out} the analog output range and $n_{integer,12}$ the number of integers in a 12-bit number.

B.2 Design choices and process

In this section the design choices and the design process are explained in more detail. First the board choice is addressed after which the external hardware will come to pass.

Board choice

First a board was chosen since it is the most significant decision. De Groot [19] had already tried to make the MEUR of the SDAC research group wireless and for that research several boards were evaluated. The *myRIO* [20] was selected. This research was unsuccessful mostly due to time restraints. However, it most likely would not have succeeded since the analog input resolution of the *myRIO* is a factor two too large. Also the *myRIO* is not Simulink compatible so it is not preferred.

In the recommendations it is stated to take a look into the *Raspberry Pi 3B*, since it has a lot more computational power. This board is worth to investigate further since it is already compatible with Simulink [21]. This board does have the drawback of not having analog and encoder inputs and analog outputs. Therefore, these need to be added with external hardware.

Also from the boards listed by De Groot [19] only the *myRIO* and the *Raspberry Pi 3B* have wireless options with exception of the *Speedgoat* which is over-sized for the MEUR. While the other boards can run standalone they do not have enough memory to record all the measurements for later download. These boards need at least:

$$M = n_{channels} \cdot r_{channel} \cdot t_{exp}/t_{sample} = 8_{channel} \cdot 2 \frac{bytes}{channel} \cdot 70s/0.001s = 1.12MB \quad (B.5)$$

Where M is the needed memory, $n_{channels}$ the minimum number of channels to measure (6DOF and 2 encoders), $r_{channel}$ the number of bytes per channel, t_{exp} the experiment duration and t_{sample} the sample time.

In conclusion the *Raspberry Pi 3B* was chosen. As stated external hardware is needed which will be addressed in the next section.

External hardware

The external hardware needs to add analog inputs and outputs as well as encoder inputs. The *Raspberry Pi 3B* needs to communicate with this hardware. The *Raspberry Pi 3B* has multiple hardware interfaces available: *SPI*, *I2C* and *serial*. For a single time step a minimum of 156bits needs to be communicated with the external hardware. Six analog inputs with 16-bits, two analog outputs with 12-bits and two encoder inputs with 18-bits. If the system runs at 1kHz this results in 156kbit/s .

This is above the bit rate of *serial* interface which runs at 115.2kbit/s . So this interface will not work.

The *I2C* interface is running faster at 400kbit/s but there will be overhead needed of at least 48bits to address one of the three external hardware chips (1 byte) and their internal registers (1 byte). This results in a minimum of bit rate of 204kbit/s leaving little overhead for the *Raspberry Pi 3B*.

Therefore, the only interface fast enough for the communication with the external hardware is the *SPI* interface, which can run at 32Mbit/s and the *Raspberry Pi 3B* even offers two *SPI* interfaces. Thus some communication can be done in parallel.

ADC

It can be concluded that the ADC should have at least six inputs of 16-bits, should be able to take in measurements at least 6kS/s and communicate using the *SPI* interface. The *ADS8688IDBT* [22] was chosen since it not only fits the requirements but also all the wishes, like the extra inputs.

Digital to Analog Converter (DAC)

The DAC should have at least two outputs of 12-bits and should be capable to run at at least 2kS/s . Again a chip was chosen that not only fits the requirements but also all the wishes, like the higher resolution, i.e. the *AD5360BSTZ* [23].

Encoder inputs

Most systems do not need an external encoder input decoder chip since often encoder signals are low frequency due to low number of counts per revolution. Therefore, normally these signals can be decoded with software that is triggered by an interrupt. However, the encoders in this setup have high number of counts per revolution so such an implementation would take up too much CPU time to count all the steps or counts will be missed. Hence a hardware solution is needed, however these chips are rare since most of the time they are not needed. Also the chips that do exist do not have either the right amount of encoder inputs, can not count large enough numbers or simply could not be ordered.

Therefore, it was chosen to use a Complex Programmable Logic Device (CPLD) to get this task done. A CPLD was preferred over a Field Programmable Gate Array (FPGA) since

it keeps it program over power cycles. First Very high speed integrated circuit Hardware Description Language (VHDL) code was written to get an estimate of which size CPLD would be needed. From this the CPLD *5M1270ZT144C4N* [24] was chosen as the minimum number of logic cell needed was estimated to be at least 667 for three inputs. Since there was room for a fourth input it was chosen to add this extra input as well. Later with testing and debugging on the real hardware it was noted that the needed number of logic cells was lower so a smaller chip could have been used. Due to limited number of prototype boards this was not altered anymore.

Final design

Now that the board and external hardware was chosen a Printed Circuit Board (PCB) was designed to house all the electronics. It not only has the external hardware and a connector for the *Raspberry Pi 3B* but also all the supporting electronics, including for example power supplies and a voltage reference.

Next a Simulink library was made to link Simulink signals with the hardware. After some debugging a redesign of the PCB deemed necessary due to limitations on one of the two *SPI* interfaces and power supply problems. Finally a working board was made.

The source files for the final design (PCB design and VHDL code) and the Simulink library can be found at [7].

Derivation ideal roll angle during cornering

The ideal roll angle for the MEUR to make during a corner is the angle at which the reaction wheel does not have to perform any work keeping the roll angle as it is. Therefore, the angle should be such that the moments resulting from the centrifugal force and gravity should cancel, as is illustrated in figure C.1. From the free body diagram the equation of motion follows as:

$$\ddot{\gamma} \cdot J_r = L \cdot m \cdot g \cdot \sin \gamma - L \cdot F_m \cdot \cos \gamma \quad (\text{C.1})$$

This equation can be rewritten into the following for a steady roll angle γ , i.e. $\ddot{\gamma} = 0$:

$$\gamma = \arctan \frac{F_m}{m \cdot g} \quad (\text{C.2})$$

Filling in the equation of centrifugal force $F_m = m \cdot v^2 / r$ gives:

$$\gamma = \arctan \frac{m \cdot v^2}{m \cdot g \cdot r} = \arctan \frac{v^2}{g \cdot r} \quad (\text{C.3})$$

Where v is the longitudinal velocity of the MEUR and r the radius of the corner.

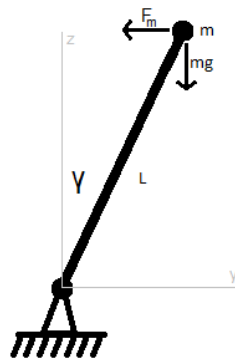


Figure C.1: Free body diagram ideal roll angle

Evaluation of the reaction wheel

In this appendix it is investigated whether the reaction wheel on the MEUR has a sufficiently large inertia. Increasing the inertia of the reaction wheel has a positive effect on the maximum recovery angle. The maximum recovery angle is the angle at which the robot is still able to return to a stable position.

D.1 Derivation

The maximum recovery angle was derived as a function of the reaction wheel inertia and a few other parameters. For this calculation it is assumed the robots start stationary at $t = 0$ in the maximum recovery angle $\theta_{r,max}$ with its reaction wheel at rest and ends at t_{end} in an upright position at rest. At the start a constant torque is applied on the reaction wheel until it reaches its maximum angular velocity, after which no more torque is exchanged.

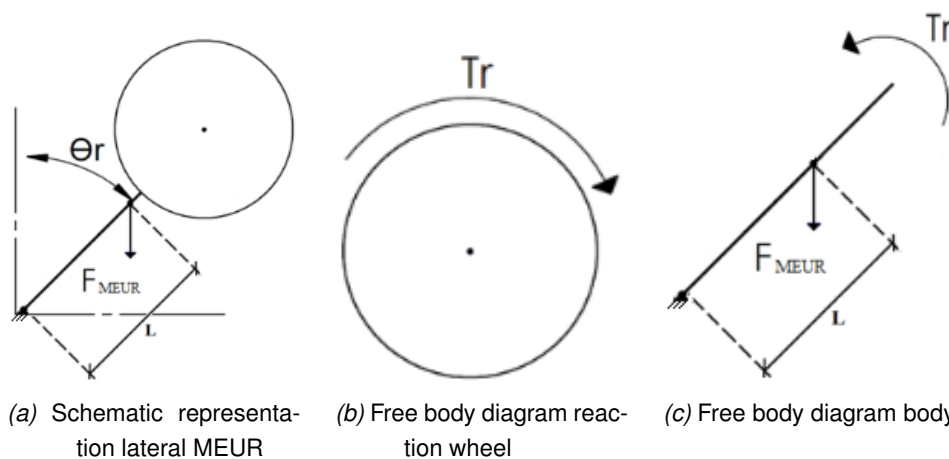


Figure D.1: Combined view: schematic representation and free body diagrams

The forces and moments acting on the reaction wheel and body are shown in figure D.1. For the reaction wheel the equation of motion becomes:

$$T_{rC} = \alpha_{RW} \cdot J_{RW} \quad (D.1)$$

Where T_{rC} is the applied motor torque from $0 \leq t < t_{max}$, α_{RW} the angular acceleration of the reaction wheel and J_{RW} the reaction wheel inertia. The equation of motion can be rewritten to:

$$\alpha_{RW} = \frac{T_{rC}}{J_{RW}} \quad (D.2)$$

Next the maximum time the motor torque can be applied is derived, from the maximum reaction wheel velocity $\omega_{RW,max}$:

$$\omega_{RW,max} = \int_0^{t_{max}} \alpha_{RW} dt = \alpha_{RW} \cdot t_{max} \quad (D.3a)$$

$$t_{max} = \frac{\omega_{RW,max}}{\alpha_{RW}} = \frac{\omega_{RW,max} \cdot J_{RW}}{T_{rC}} \quad (D.3b)$$

The equation of motion of the body is:

$$F_{MEUR} \cdot L \cdot \sin(\theta_r(t)) - T_r(t) = \alpha_r(t) \cdot J_r \quad (D.4)$$

Where T_r is the applied motor torque. For which the function is:

$$T_r(t) = \begin{cases} 0 & t < 0 \\ T_{rC} & t \geq 0 \end{cases} + \begin{cases} 0 & t < t_{max} \\ -T_{rC} & t \geq t_{max} \end{cases} \quad (D.5)$$

Using $F_{MEUR} = m_r \cdot g$, where m_r is the body mass, the equation of motion of the body becomes:

$$m_r \cdot g \cdot L \cdot \sin(\theta_r(t)) - T_r(t) = \alpha_r(t) \cdot J_r \quad (D.6)$$

Using the Laplace transform on the equation of motion of the body with the initial conditions and assuming small angles results in:

$$s^2 \cdot \theta_r \cdot J_r - J_r \cdot s \cdot \theta_{r,max} \approx m_r \cdot g \cdot L \cdot \theta_r - \frac{T_{rC}}{s} (1 - e^{-t_{max}s}) \quad (D.7)$$

Solving for the body angle results in:

$$\theta_r \left(s^2 - \frac{m_r \cdot g \cdot L}{J_r} \right) = s \cdot \theta_{r,max} - \frac{T_{rC}}{J_r \cdot s} (1 - e^{-t_{max}s}) \quad (D.8a)$$

$$\theta_r(s) = \frac{s \cdot \theta_{r,max}}{\left(s^2 - \frac{m_r \cdot g \cdot L}{J_r} \right)} - \frac{1}{s} \frac{\frac{T_{rC}}{J_r}}{\left(s^2 - \frac{m_r \cdot g \cdot L}{J_r} \right)} (1 - e^{-t_{max}s}) \quad (D.8b)$$

This equation can be rewritten to:

$$\theta_r(s) = \theta_{r,max} \frac{s}{\left(s^2 - \frac{m_r \cdot g \cdot L}{J_r} \right)} - \frac{\frac{T_{rC}}{J_r}}{\sqrt{\frac{m_r \cdot g \cdot L}{J_r}}} \frac{1}{s} \frac{\sqrt{\frac{m_r \cdot g \cdot L}{J_r}}}{\left(s^2 - \frac{m_r \cdot g \cdot L}{J_r} \right)} (1 - e^{-t_{max}s}) \quad (D.9)$$

Next the inverse Laplace transform is used:

$$\theta_r(t) = \theta_{r,max} \cosh\left(\sqrt{\frac{m_r \cdot g \cdot L}{J_r}} t\right) - \frac{\frac{T_r C}{J_r}}{\sqrt{\frac{m_r \cdot g \cdot L}{J_r}}} \left(\int_0^t \sinh\left(\sqrt{\frac{m_r \cdot g \cdot L}{J_r}} \tau\right) d\tau - \int_{-t_{max}}^{t-t_{max}} \sinh\left(\sqrt{\frac{m_r \cdot g \cdot L}{J_r}} \tau\right) d\tau \right) \quad (D.10)$$

Solving the integrals results in:

$$\theta_r(t) = \theta_{r,max} \cosh\left(\sqrt{\frac{m_r \cdot g \cdot L}{J_r}} t\right) - \frac{\frac{T_r C}{J_r}}{\sqrt{\frac{m_r \cdot g \cdot L}{J_r}}} \frac{\cosh\left(\sqrt{\frac{m_r \cdot g \cdot L}{J_r}} t\right)}{\sqrt{\frac{m_r \cdot g \cdot L}{J_r}}} + \frac{\frac{T_r C}{J_r}}{\sqrt{\frac{m_r \cdot g \cdot L}{J_r}}} \frac{1}{\sqrt{\frac{m_r \cdot g \cdot L}{J_r}}} + \frac{\frac{T_r C}{J_r}}{\sqrt{\frac{m_r \cdot g \cdot L}{J_r}}} \frac{\cosh\left(\sqrt{\frac{m_r \cdot g \cdot L}{J_r}} (t - t_{max})\right)}{\sqrt{\frac{m_r \cdot g \cdot L}{J_r}}} - \frac{\frac{T_r C}{J_r}}{\sqrt{\frac{m_r \cdot g \cdot L}{J_r}}} \frac{\cosh\left(\sqrt{\frac{m_r \cdot g \cdot L}{J_r}} t_{max}\right)}{\sqrt{\frac{m_r \cdot g \cdot L}{J_r}}} \quad (D.11)$$

$$= \theta_{r,max} \cosh\left(\sqrt{\frac{m_r \cdot g \cdot L}{J_r}} t\right) - \frac{T_r C}{m_r \cdot g \cdot L} \cosh\left(\sqrt{\frac{m_r \cdot g \cdot L}{J_r}} t\right) + \frac{T_r C}{m_r \cdot g \cdot L} + \frac{T_r C}{m_r \cdot g \cdot L} \cosh\left(\sqrt{\frac{m_r \cdot g \cdot L}{J_r}} (t - t_{max})\right) - \frac{T_r C}{m_r \cdot g \cdot L} \cosh\left(\sqrt{\frac{m_r \cdot g \cdot L}{J_r}} t_{max}\right) \quad (D.12)$$

$$= (\theta_{r,max} - A) \cosh(B \cdot t) + A + A \cosh(B \cdot (t - t_{max})) - A \cdot C \quad (D.13)$$

Where:

$$A = \frac{T_r C}{m_r \cdot g \cdot L} \quad (D.14)$$

$$B = \sqrt{\frac{m_r \cdot g \cdot L}{J_r}} \quad (D.15)$$

$$C = \cosh(-B \cdot t_{max}) \quad (D.16)$$

$$S = \sinh(-B \cdot t_{max}) \quad (D.17)$$

The time derivative of $\theta_r(t)$ becomes:

$$\dot{\theta}_r(t) = (\theta_{r,max} - A)B \sinh(B \cdot t) + A \cdot B \sinh(B \cdot (t - t_{max})) \quad (D.18)$$

At t_{end} the body angle and velocity are zero, using this on $\dot{\theta}_r(t)$:

$$\dot{\theta}_r(t_{end}) = (\theta_{r,max} - A)B \sinh(B \cdot t_{end}) + A \cdot B \sinh(B \cdot (t_{end} - t_{max})) = 0 \quad (D.19)$$

Hence:

$$(\theta_{r,max} - A)B \sinh(B \cdot t_{end}) + A \cdot B \sinh(B \cdot t_{end}) \cosh(-B \cdot t_{max}) + A \cdot B \cosh(B \cdot t_{end}) \sinh(-B \cdot t_{max}) = 0 \quad (D.20)$$

$$(\theta_{r,max} + A(C - 1))B \sinh(B \cdot t_{end}) + A \cdot S \cdot B \cosh(B \cdot t_{end}) = 0 \quad (D.21)$$

Solving for $B \cdot t_{end}$ results in:

$$B \cdot t_{end} = \operatorname{arctanh} \left(- \frac{A \cdot S}{\theta_{r,max} + A(C - 1)} \right) \quad (D.22)$$

The function for $\theta_r(t)$, equation D.13, can be rewritten to:

$$\begin{aligned} \theta_r(t) = & (\theta_{r,max} - A) \cosh(B \cdot t) + A \cosh(B \cdot t) \cosh(-B \cdot t_{max}) + \\ & A \sinh(B \cdot t) \sinh(-B \cdot t_{max}) + A(1 - C) \end{aligned} \quad (D.23)$$

$$= (\theta_{r,max} + A(C - 1)) \cosh(B \cdot t) + A \cdot S \sinh(B \cdot t) + A(1 - C) \quad (D.24)$$

Filling the result of $B \cdot t_{end}$ into this equation and using that the position is zero at t_{end} results in:

$$\begin{aligned} \theta_r(t_{end}) = & (\theta_{r,max} + A(C - 1)) \cosh \left(\operatorname{arctanh} \left(- \frac{A \cdot S}{\theta_{r,max} + A(C - 1)} \right) \right) + \\ & A \cdot S \sinh \left(\operatorname{arctanh} \left(- \frac{A \cdot S}{\theta_{r,max} + A(C - 1)} \right) \right) + A(1 - C) = 0 \end{aligned} \quad (D.25)$$

Solving the equation for $\theta_{r,max}$ with Matlab symbolic toolbox results into the following three solutions:

$$\theta_{r,max} = \left[\begin{array}{l} A \cdot \left(\sqrt{2} \cdot \cosh(B \cdot t_{max}) \sqrt{\frac{-1}{\cosh(B \cdot t_{max}) - \cosh(B \cdot t_{max})^2} - 1} \right) \cdot (\cosh(B \cdot t_{max}) - 1) \\ -A \cdot \left(\sqrt{2} \cdot \cosh(B \cdot t_{max}) \sqrt{\frac{-1}{\cosh(B \cdot t_{max}) - \cosh(B \cdot t_{max})^2} + 1} \right) \cdot (\cosh(B \cdot t_{max}) - 1) \\ \frac{-A \cdot (2 \cdot \cosh(B \cdot t_{max}) + \sinh(B \cdot t_{max})) \cdot (\cosh(B \cdot t_{max}) - 1)}{\sinh(B \cdot t_{max})} \end{array} \right] \quad (D.26)$$

With the parameters, see table D.1, of the current MEUR the three solutions are calculated to be:

$$\theta_{r,max} = \left[\begin{array}{l} 0.0438 \text{rad} \approx 2.313^\circ \\ -0.0471 \text{rad} \approx -2.700^\circ \\ -0.0472 \text{rad} \approx -2.708^\circ \end{array} \right]$$

Since only the first solution is positive that solution is the maximum recovery angle.

Parameter	Value
m_r	7.22kg
L	0.227m
J_r	$m_r \cdot L^2 = 0.372 \text{kg} \cdot \text{m}^2$
$\omega_{RW,max}$	22.14rad/s
J_{RW}	0.0048kg · m ²
T_{rC}	4.51Nm

Table D.1: MEUR parameters

D.2 Validation

Using a simulation the result is verified. In Simulink a model was made, see figure D.2. The results from the simulation, see figure D.3, shows that the calculation is a slight overestimation, because it nearly misses the zero position. However, it is a good estimation. Also it does not matter the result is not as exact as one would expect with the analytical calculation since the result is more of an indication of how well the MEUR performs.

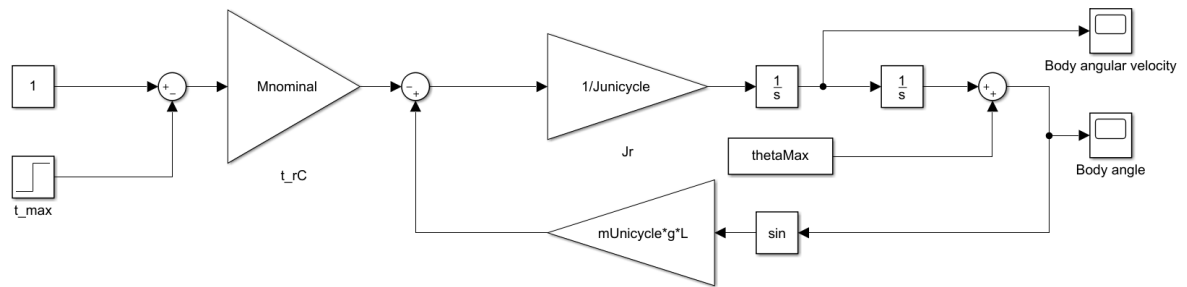


Figure D.2: Maximum recovery angle validation simulation model

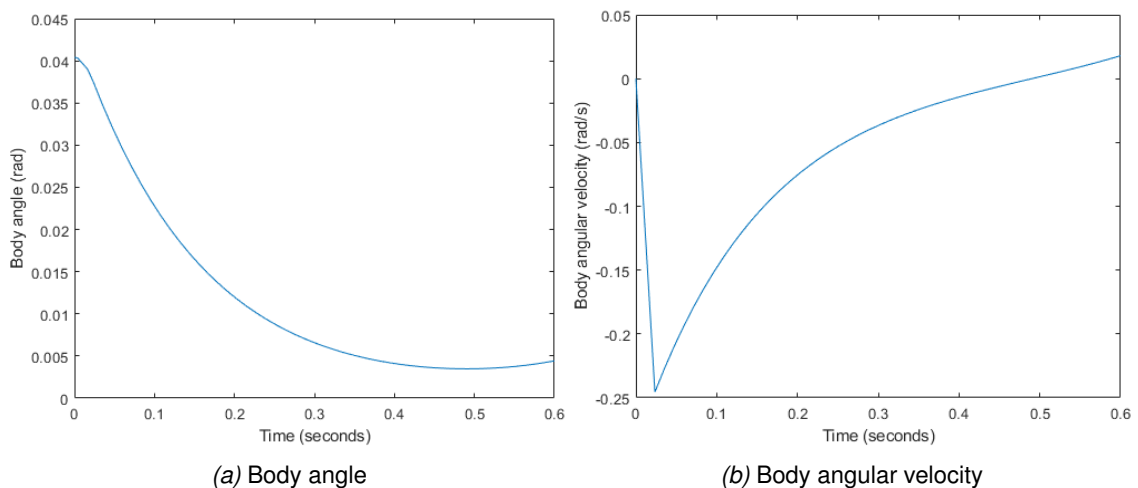


Figure D.3: Maximum recovery angle validation simulation

The maximum recovery angle is considered to be too small since it places high accuracy demands on the starting positioning, as also was noticed during experiments. Furthermore, this small maximum recovery angle limits the saturation of the jaw SiMo and thus the turning control. Also it should be noted that the MEUR becomes less resistant to disturbances when the maximum recovery angle is small. Thus, the reaction wheel inertia should be increased, since this will lead to a larger recovery angle. This can be done by either increasing its mass or its radius or both. Increasing either will also have an effect on body inertia and center of mass. This is further investigated in the next section.

It should be noted that in the derivation friction was ignored. This will lead to an over-estimation of the maximum recovery angle since the friction will act as damper between the reaction wheel and the rest of the MEUR. Also, the maximum recovery angle will most likely be smaller due to the controller not being aggressive enough, since derivation is only valid for constant high torque.

D.3 Reaction wheel alteration

To get a better understanding of the effect of all possible reaction wheel alterations several parameters are recalculated. First the MEUR rotational inertia is split into two parts, namely the contribution of the reaction wheel and its drivetrain $J_{RW,MEUR}$ and the rest of the MEUR J_{MEUR} :

$$J_r = J_{RW,MEUR} + J_{MEUR} \quad (D.27)$$

Where:

$$J_{RW,MEUR} = (m_{RW} + m_{dt}) \cdot L_{RW}^2 \quad (D.28)$$

Where m_{RW} is the mass of the reaction wheel, m_{dt} the mass of its drivetrain and L_{RW} is the distance from the ground to the center of the reaction wheel axis. Which can be calculated with:

$$L_{RW} = L_{RW,c} + r_{RW} \quad (D.29)$$

Where $L_{RW,c}$ is the clearance distance between the ground and r_{RW} the reaction wheel and the reaction wheel. The mass of the MEUR can be split into two parts. Namely the mass of the body m_{MEUR} and the mass of the reaction wheel m_{RW} , thus the following holds:

$$m_r = m_{MEUR} + m_{RW} \quad (D.30)$$

The distance of center of mass L can be calculated by:

$$L = \frac{L_{MEUR} \cdot m_{MEUR} + L_{RW} \cdot m_{RW}}{m_r} \quad (D.31)$$

Where L_{MEUR} is the distance of the center of mass of the body without the reaction wheel contribution. The reaction wheel inertia J_{RW} is calculated with the following:

$$J_{rw} = m_{RW} \cdot r_{RW}^2 \quad (D.32)$$

In table D.2 the extra needed parameters are given for the MEUR. Next the solution for the maximum recovery angle is re-evaluated for other values for r_{RW} and m_{RW} . Variable r_{RW} is varied between $0.1m$ and $0.35m$ and variable m_{RW} between $0.3kg$ and $1kg$. Figure D.4 shows the result. From this result it can be concluded that increasing the reaction wheel inertia by either its mass or its radius or both will lead to a larger recovery angle. Increasing both is the most effective. Thus this is recommended.

With this calculation the effect of need for a higher and thus heavier frame for a larger radius reaction wheel is not included.

Parameter	Value
m_{dt}	$1.37kg$
$L_{RW,c}$	$0.253m$
$r_{RW,initial}$	$0.115m$
$m_{RW,initial}$	$J_{RW}/r_{RW,initial}^2 = 0.363kg$
$J_{RW,MEUR,initial}$	$(m_{RW,initial} + m_{dt}) \cdot (L_{RW,c} + r_{RW,initial})^2 = 0.235kg \cdot m^2$
J_{MEUR}	$J_r - J_{RW,MEUR,initial} = 0.137kg \cdot m^2$
m_{MEUR}	$m_r - m_{RW,initial} = 6.86kg$
L_{MEUR}	$(L \cdot m_r - L_{RW,initial} \cdot m_{RW,initial})/m_{MEUR} = 0.220m$

Table D.2: MEUR extra parameters

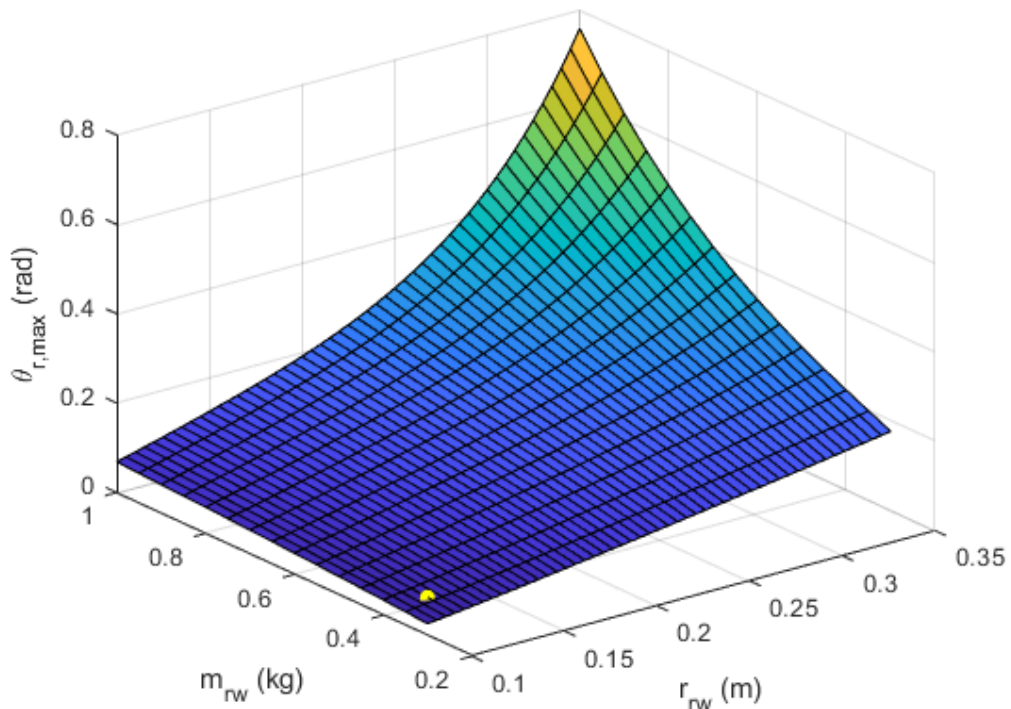


Figure D.4: Reaction wheel alterations, current reaction wheel marked with yellow dot